The Astrophysical Journal, 970:149 (27pp), 2024 August 1 https://doi.org/10.3847/1538-4357/ad4ce2

Galaxy and Mass Assembly (GAMA): Stellar-to-dynamical Mass Relation. II. Peculiar Velocities

M. Burak Dogruel[1], Edward N. Taylor[1], Michelle Cluver[1,2], Matthew Colless[3,4], Anna de Graaff[5], Alessandro Sonnenfeld[6], John R. Lucey[7], Francesco D'Eugenio[8,9], Cullan Howlett[10], and Khaled Said[10]
[1] Centre for Astrophysics and Supercomputing, Swinburne University of Technology, Hawthorn, VIC 3122, Australia; bdogruel@swin.edu.au
[2] Department of Physics and Astronomy, University of the Western Cape, Robert Sobukwe Road, Bellville, 7535, South Africa
[3] Research School of Astronomy and Astrophysics, Australian National University, Canberra, ACT 2611, Australia
[4] ARC Centre of Excellence for All Sky Astrophysics in 3 Dimensions (ASTRO 3D), Canberra, ACT 261, Australia
[5] Max-Planck-Institut für Astronomie, Königstuhl 17, D-69117, Heidelberg, Germany
[6] Department of Astronomy, School of Physics and Astronomy, Shanghai Jiao Tong University, Shanghai 200240, People's Republic of China
[7] Centre for Extragalactic Astronomy, Durham University, Durham DH1 3LE, UK
[8] Kavli Institute for Cosmology, University of Cambridge, Madingley Road, Cambridge, CB3 0HA, UK
[9] Cavendish Laboratory—Astrophysics Group, University of Cambridge, 19 JJ Thomson Avenue, Cambridge, CB3 0HE, UK
[10] School of Mathematics and Physics, The University of Queensland, Brisbane, QLD 4072, Australia
Received 2023 July 26; revised 2024 May 1; accepted 2024 May 15; published 2024 July 26

Abstract

Empirical correlations connecting starlight to galaxy dynamics (e.g., the fundamental plane (FP) of elliptical/quiescent (Q) galaxies and the Tully–Fisher relation of spiral/star-forming (SF) galaxies) provide cosmology-independent distance estimation and are central to local Universe cosmology. In this work, we introduce the mass hyperplane (MH), which is the stellar-to-dynamical mass relation ($M_\star/M_{\rm dyn}$) recast as a linear distance indicator. Building on recent FP studies, we show that both SF and Q galaxies follow the same empirical MH, then use this to measure the peculiar velocities (PVs) for a sample of 2496 galaxies at $z < 0.12$ from GAMA. The limiting precision of MH-derived distance/PV estimates is set by the intrinsic scatter in size, which we find to be ≈0.1 dex for both Q and SF galaxies (when modeled independently) and ≈0.11 dex when all galaxies are modeled together, showing that the MH is as good as the FP. To empirically validate our framework and distance/PV estimates, we compare the inferred distances to groups as derived using either Q or SF galaxies. A good agreement is obtained with no discernible bias or offset, having a scatter of ≈0.05 dex ≈12% in distance. Further, we compare our PV measurements for the Q galaxies to the previous PV measurements of the galaxies in common between GAMA and the Sloan Digital Sky Survey, which shows similarly good agreement. Finally, we provide comparisons of PV measurements made with the FP and the MH, then discuss possible improvements in the context of upcoming surveys such as the 4MOST Hemisphere Survey.

Unified Astronomy Thesaurus concepts: Galaxy distances (590); Scaling relations (2031); Astrostatistics techniques (1886); Cosmology (343); Galaxy properties (615)

1. Introduction

1.1. Peculiar Velocities

Redshift-independent distances inferred via empirical, statistical correlations are central to cosmology. In the local Universe ($z \lesssim 0.1$), galaxy scaling relations are particularly useful as a tool for measuring deviations of galaxy velocities from the Hubble–Lemaître law for the expansion of the Universe (Hubble flow). To first order, cosmological expansion is seen locally as apparent recession velocities proportional to their comoving distance: $V \equiv cz \approx H_0 D$ (Hubble 1929), where c is the speed of light, z is the redshift, D is the comoving distance (i.e., the radial distance), and H_0 is the current expansion rate of the Universe; i.e., the Hubble parameter. Deviations from the cosmic expansion are caused by the inhomogeneities in the matter distribution and they give rise to the peculiar velocities (PVs; $V_{\rm pec}$) of galaxies: $1 + z_{\rm obs} = (1 + z_H)(1 + z_{\rm pec})$ (Harrison 1974) where $z_{\rm obs}$ is the observed redshift, z_H is the cosmological/comoving redshift due to the Hubble flow, $z_{\rm pec}$ is the peculiar redshift with $V_{\rm pec} = cz_{\rm pec}$ and $z_H \approx H_0 D(z_H)/c$. In this picture, $z_{\rm obs}$ is the only observable, thus known quantity, while the true comoving distance at the cosmological redshift, $D(z_H)$ and $V_{\rm pec}$ are unknown but desired quantities.

The crucial importance of PVs in cosmological studies is better understood by tracing the origins of PV. The small anisotropy in the cosmic microwave background (CMB) already shows the existence of density inhomogeneities. According to the large-scale structure formation and growth theory, these tiny density perturbations grow over time because of their self-gravity and generate local gravitational fields due to local density fluctuations (i.e., the differences between overdense and underdense regions creating density contrasts). These gravitational fields drive the matter flow and generate PVs. Thus, especially at low redshifts, PVs enable cosmography (e.g., Springob et al. 2014; Tully et al. 2014; Graziani et al. 2019), bulk flow measurements (e.g., Qin et al. 2021; Howlett et al. 2022), fitting cosmological parameters such as the growth rate of structure, mass fluctuation amplitude within $8\,{\rm hr}^{-1}$ Mpc radius spheres (σ_8; e.g., Turnbull et al. 2012; Carrick et al. 2015; Said et al. 2020), and even tests of the standard ΛCDM model and general relativity (e.g., Adams & Blake 2017; Howlett et al. 2017; Said et al. 2020).

On the other hand, direct calculation of PVs requires measurements of both redshifts and redshift-independent distances. Some of the well-known distance indicators that are widely used in PV studies are the period–luminosity relation of Cepheid variables (Leavitt & Pickering 1912), Type Ia supernovae (SNe Ia; Phillips 1993), the Tully–Fisher relation (TFR) for disk galaxies (Tully & Fisher 1977), and the fundamental plane (FP; Djorgovski & Davis 1987; Dressler et al. 1987) for elliptical galaxies and spheroids. Even though Cepheids provide the most accurate and precise extragalactic distances (e.g., Riess et al. 2016, 2021), they are only useful to distances short enough ($\lesssim$25 Mpc) to be able to discern them within a galaxy in the first place. While SNe Ia provide precise distances (Howlett et al. 2017; Koda et al. 2014; Scolnic et al. 2018, and references therein) even for $z > 1$, their rarity in the local Universe and observational challenges limit SNe Ia distances to relatively small numbers of galaxies ($\sim$1000 galaxies).

1.2. Dynamical Scaling Relations

Empirical galaxy scaling relations that relate distance-dependent properties (e.g., physical size, luminosity) to distance-independent intrinsic properties (e.g., stellar kinematics, surface brightness, color) are much easier to measure, and galaxies that obey these relations are quite abundant. For these reasons, the TFR and the FP have been the pillars of PV studies (cf., the statistical measurement of PVs via redshift space distortions for a sample of galaxies; Kaiser 1987) thanks to their availability and sample sizes. Even though both relations are seen to be remarkably tight, with modern data, the intrinsic scatters around these relations are the limiting factor in the precision of distance measurements/estimates: $\sim$0.1 dex or 20%–25%. In fact, these large errors in PVs have become the characteristic feature of PV surveys (Watkins & Feldman 2015), and these errors grow linearly with increasing distance. This is another fundamental reason why PVs are most useful at low redshifts ($z \sim 0.1$).

The traditional FP of elliptical/early-type galaxies is expressed in terms of luminosity with surface brightness, $\langle I_e \rangle \equiv L/2\pi R_e^2$;

$$\log R_e = a \log \sigma_0 + b \log \langle I_e \rangle + c \tag{1}$$

and can be referred to as the luminosity fundamental plane (LFP). Here, R_e is the physical effective radius (within which half of the luminosity is emitted) in units of h^{-1} kpc, where h is the scaled Hubble constant as $H_0 = 100h$ km s^{-1} Mpc^{-1}, σ_0 is the central velocity dispersion in kilometers per second, $\langle I_e \rangle$ is the surface brightness in $L_\odot$ pc^{-2} and the subscript e denotes the measurements made within the effective radius. In terms of directly observed properties—angular effective radius (θ_e), apparent magnitude (m_λ), and redshift—the LFP parameters for a band λ are

$$\begin{aligned} R_e &= \theta_e D_A, \\ \log \langle I_e \rangle_\lambda &= 0.4(M_\odot^\lambda - \mu_e^{\rm cor}) + 8.629, \\ \mu_e^{\rm cor} &= m_\lambda - A_\lambda - k_\lambda(z_{\rm obs}) + 2.5 \log(2\pi\theta_e^2) \\ &\quad - 2.5 \log (1 + z_{\rm obs})^4. \end{aligned} \tag{2}$$

Here, D_A is the angular diameter distance, $M_\odot^\lambda$ is the absolute magnitude of the Sun, $\mu_e^{\rm cor}$ is the surface brightness in magnitudes per square arcseconds corrected for galactic extinction (A_λ), bandpass stretching ($k_\lambda(z_{\rm obs})$; correcting magnitudes to rest frame), and surface brightness dimming ($\log(1 + z_{\rm obs})^4$). The form in Equation (1) separates the distance-dependent quantity, $\log R_e$, from the distance-independent quantities σ_0 and $\langle I_e \rangle$.[11] Multiplying $\langle I_e \rangle$ by the stellar mass-to-light ratio ($M_\star/L$) estimated from spectral energy distribution (SED) modeling gives the surface stellar-mass density within R_e, denoted with $\Sigma_\star$: $(M_\star/L)\langle I_e \rangle = M_\star/(2\pi R_e^2) \equiv \Sigma_\star$. Thus, when $\Sigma_\star$ replaces $\langle I_e \rangle$ in the LFP (Equation (1)), we obtain what might be called the stellar-mass fundamental plane (SMFP):

$$\log R_e = \alpha \log \sigma_e + \beta \log \Sigma_\star + \gamma. \tag{3}$$

1.3. Unification and Generalization of Dynamical Scaling Relations

There have been some attempts at finding a universal fundamental plane (UFP), in the sense that it is applicable to all types of galaxies. Zaritsky et al. (2008) and Aquino-Ortíz et al. (2020) have shown that it is possible to define a UFP at low redshifts, such that both elliptical and spiral galaxies reside on the same plane, with

$$\log\left(\frac{M_{\rm dyn}}{L}\right)_e \equiv \log \Upsilon_e = \log(S_{0.5}^2) - \log\langle I_e \rangle - \log R_e + C. \tag{4}$$

In this relation, Υ_e is the dynamical mass-to-light ratio within R_e and $S_K^2 = KV_{R_e}^2 + \sigma_e^2$ is the total velocity parameter (Weiner et al. 2006), where K is assumed to be constant and is usually taken to be 0.5 (Cortese et al. 2014). $S_{0.5}$ encompasses rotational velocity (V_{R_e}) and velocity dispersion within R_e (σ_e). These definitions make it clear that a UFP is possible when we account for both mass-to-light ratio and rotational velocity.

Bezanson et al. (2015) have shown that star-forming (SF) and quiescent (Q) galaxies lie on the same SMFP for $z \sim 0$ galaxies from the Sloan Digital Sky Survey (SDSS), albeit in different regions of that plane. Furthermore, using the data from LEGA-C, de Graaff et al. (2020) have definitively shown that the SMFP relation is the same up to $z \sim 1$. Even more interestingly, again using LEGA-C data, de Graaff et al. (2021) have demonstrated that both SF and Q galaxies not only share the same SMFP, but they also share the same LFP, just with different zero-points and so again in different regions of the plane. In both of these studies, authors have found larger intrinsic scatter for SF galaxies.

These results are, in fact, not shocking discoveries. Velocity dispersion, when measured within the effective radius, σ_e, is a good approximation to the luminosity-weighted rms of the line-of-sight velocity inside R_e, and thus, includes both rotation and dispersion (Cappellari et al. 2006, 2013 or see the review by Courteau et al. 2014). Therefore, using σ_e instead of σ_0 in the LFP and the SMFP (Equations (1) and 3) will suffice to approximately account for rotational velocity, as required in the UFP of Zaritsky et al. (2008) and Aquino-Ortíz et al. (2020).

Furthermore, these results raise a rather obvious question: Why should we discard spiral/SF/late-type/blue galaxies from a PV study carried out with the FP? Or, what really happens if we include those galaxies in such a study? In this paper, we are

[11] Even though $\langle I_e \rangle$ being in units of $L_\odot$ pc^{-2} might create a confusion as to its distance independence, as seen from Equation (2), it scales with the surface brightness dimming, $(1 + z_{\rm obs})^4$, and requires $k_\lambda(z_{\rm obs})$; however, $z_{\rm obs}$ is directly observable.

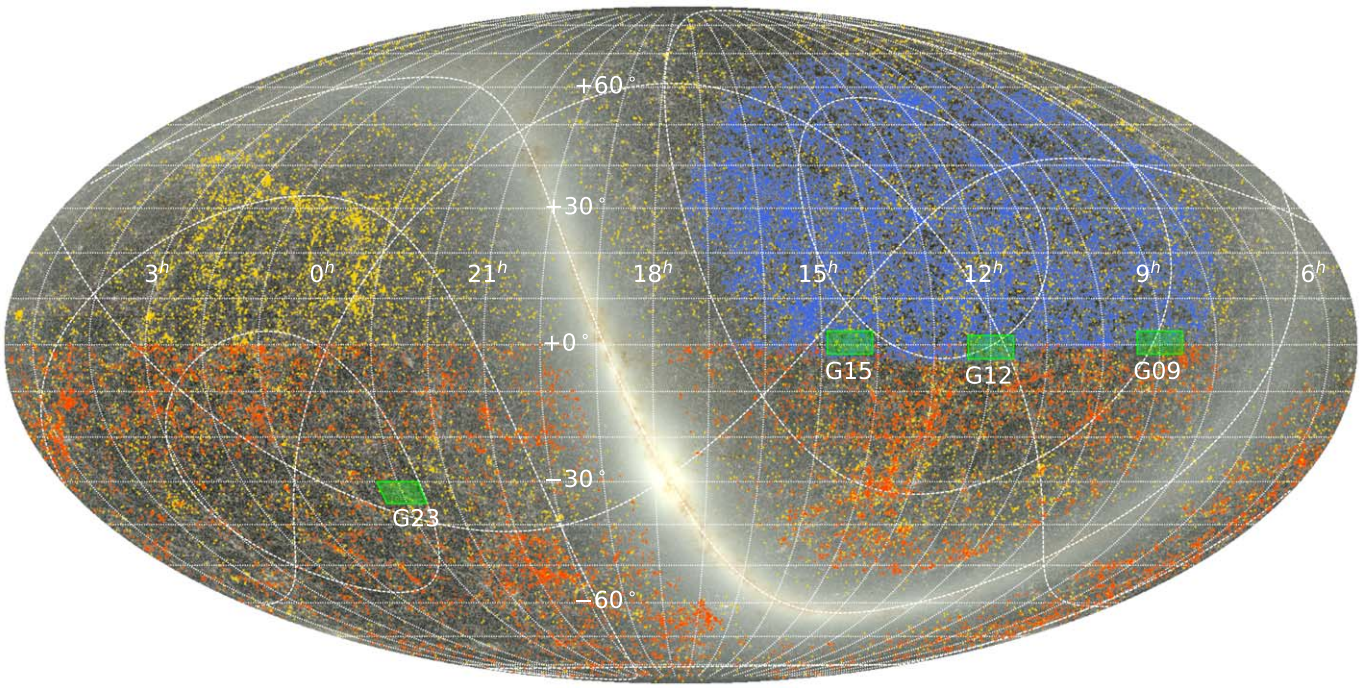

Figure 1. Distribution of the GAMA sample (green) in equatorial coordinates in comparison to 6dFGS (orange), CF4 (yellow), and SDSS (blue) shown in Mollweide projection, underlain by the Two Micron All Sky Survey image of the Milky Way. The final GAMA PV sample consists of regions G09, G12, and G15, including 1489 SF and 1046 Q galaxies (a total of 2535 galaxies).

addressing these naturally arising questions in the wake of recently reached conclusions from Bezanson et al. (2015) and de Graaff et al. (2021) that we summarized above.

This work is structured as follows: We present our sample selection from GAMA and a description of our methodology in Section 2. We give the fitting results of the FP and the MH, along with the investigation of possible systematics in Section 3. We then present the main focus of this paper; measuring redshift-independent distances (and thus PVs) for GAMA in Section 4. Finally, we summarize our results and discuss future work in Section 5.

Throughout this work, we assume a flat ΛCDM cosmology with $\Omega_m = 0.3$, $\Omega_\Lambda = 0.7$, and $H_0 = 100h$ km s^{-1} Mpc^{-1}. Unless otherwise stated, redshifts should be understood as *flow corrected* following Baldry et al. (2012), i.e., using the Tonry et al. (2000) model and tapering to a CMB-centric frame for $z > 0.03$.

2. Data and Method

2.1. GAMA Sample Selection

The sky coverage of our GAMA PV sample in equatorial coordinates is presented in Figure 1 in comparison to some of the previous large-scale PV studies carried out in the last decade: 6° Field Galaxy Survey (6dFG, using the FP; Springob et al. 2014), Cosmicflows-4 (CF4; using TFR; Kourkchi et al. 2020), and SDSS, using the FP (Howlett et al. 2022).

We use the same mass-limited sample drawn from GAMA, as detailed in Dogruel et al. (2023). In summary, the adopted selection criteria are as follows:

1. Spectroscopic redshift quality flag $nQ \geqslant 3$ in the range of $z < 0.12$,[12]
2. Stellar masses, $\log M_\star/M_\odot > 10.3$, and
3. Velocity dispersions, $60 < \sigma_e[\mathrm{km\,s^{-1}}] < 450$ with uncertainties $\varepsilon_\sigma < 0.25\sigma_e + 25$.

In addition to these selection criteria, we also apply a cut on the projected axis ratio ($q \equiv b/a$) and, as in Howlett et al. (2022), we select galaxies with $q > 0.3$ to limit our sample to exclude galaxies close to edge-on. We further elaborate on this choice of 0.3 in Section 3.4. For now, we note that there is the potential for complex systematics, especially for disk galaxies, arising from this selection, but that none of our results or conclusions change significantly if change our selection to, for example, $q > 0.5$ (see also Figure 2). Thus, it does not affect our main model (Section 2.2.1), though it causes a sizable reduction in the number of galaxies in our sample (from 2850 galaxies to 2535).

Before moving on, it is imperative to explain our approach to aperture corrections for the velocity dispersions. As stated in Dogruel et al. (2023), GAMA velocity dispersion measurements have been calibrated to match those of SDSS, in which spectra have been taken using fibers with an aperture radius of $\theta_{\rm ap} = 1\farcs5$. For ∼84% of galaxies in our sample, the θ''_e exceeds this value, which means that for these galaxies, the velocity dispersions measured through fibers might not reflect its value within the effective radius. In order to calculate the velocity dispersions within the effective radii, σ_e, we use the aperture correction in the form derived by Jorgensen et al. (1995) and Cappellari et al. (2006): $\sigma_{\rm ap}/\sigma_e = (\theta_{\rm ap}/\theta_e)^\alpha$. Adopting the value $\alpha = -0.033 \pm 0.003$ derived by de Graaff et al. (2021) for SDSS, we find that the mean of this correction to σ_e is ∼2%, corresponding to the corrections for $\log \sigma_e$ with a mean of 0.008 dex and a standard deviation of 0.008 dex. Therefore, as in Taylor et al. (2010), it is safe to say this correction does not play an important role in our results.

[12] The stellar-mass selection results in galaxies with $z > 0.01$ being selected.

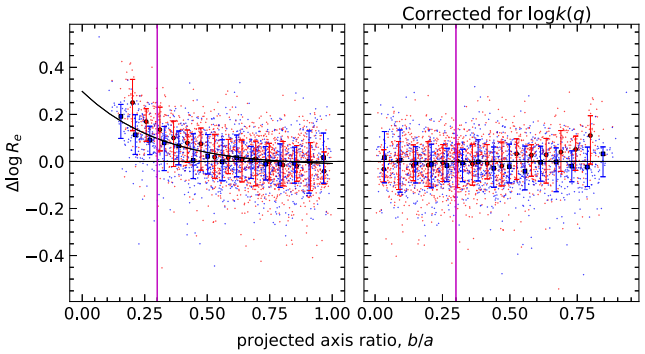

Figure 2. Residuals in the r-direction as a function of axis ratio with symbols and colors being the same as Figure 3. The left-hand panel shows the residuals before the $k(q)$ correction was applied to R_e. Here, the smooth black curve shows the $\log k(q)$ from van der Wel et al. (2022). The right-hand panel shows the residuals corrected for $k(q)$. The vertical magenta line shows the $q = 0.3$ lower limit adopted for our sample selection.

We make the distinction between Q and SF galaxies based on the equivalent width of Hα emission lines, which is taken to be $W_{\mathrm{H}\alpha} < 1$Å for quiescent (Q) galaxies (Howlett et al. 2022) and for Q galaxies $W_{\mathrm{H}\alpha} \geqslant 1$Å, which naturally divides the two populations seen in the M_*–$W_{\mathrm{H}\alpha}$ diagram (see Dogruel et al. 2023).

A common practice in PV studies conducted with the TFR and the FP is to use the group redshifts (z_{group}), instead of individual galaxy redshifts, to calculate R_e for galaxies that are members of galaxy groups/clusters. The z_{group} is usually taken to be the median redshift of individual group/cluster members. This practice is adopted for partially reducing the effects of nonlinear motion stemming from intra-group/cluster PVs (e.g., Hong et al. 2014; Springob et al. 2014; Howlett et al. 2017). In this work, though, we still use the individual CMB-frame redshifts for all galaxies in our sample so that we can then calculate the group/cluster averaged distances. It should be pointed out here that, in light of Calcino & Davis (2017), we use heliocentric[13] redshifts for conversions from comoving distance (D_C) to angular diameter (D_A) and luminosity distances (D_L). We obtain the group information from the data management units (DMUs) named `G3CGalv10` and `G3CFoFGroupv10` (Robotham et al. 2011), and we find that 1794 of the 2535 galaxies in our GAMA sample reside in 180 unique groups.

2.2. Method

2.2.1. Bayesian Framework

An extensive analytical description of the model is given in Dogruel et al. (2023). Briefly, we define an eight-dimensional space of galaxy properties, namely, $r \equiv \log R_e$ [h^{-1} kpc], $s \equiv \log \sigma_e$ [kms^{-1}], $i \equiv \log \langle I_e \rangle$ [$L_\odot$pc^{-2}], $m^* \equiv \log M_\star [M_\odot]$, $\ell \equiv \log L [L_\odot]$, $c = (g-i)_{\mathrm{rest}}$ rest-frame color, $\nu \equiv \log n$, and $m^d \equiv \log M_{\mathrm{dyn}} [M_\odot]$. Then, in a Bayesian framework, we model the distribution of galaxies in this 8D parameter space, $\hat{\mathbf{y}} = (\boldsymbol{r}, \boldsymbol{s}, \boldsymbol{i}, \boldsymbol{m}^*, \boldsymbol{\ell}, \boldsymbol{c}, \boldsymbol{\nu}, \boldsymbol{m}^{\boldsymbol{d}})$, as a Gaussian mixture model with two components: (i) the core model for the underlying distribution as an 8D Gaussian with mean $\bar{\mathbf{y}}$ and covariance matrix $\boldsymbol{\Sigma}$, convolved with observational errors: $\hat{\mathbf{y}}_\mathbf{j} \sim \mathcal{N}(\bar{\mathbf{y}}, \boldsymbol{\Sigma} + \mathbf{E_j})$, (ii) the outlier model, in which outliers are parameterized as a fraction ($f_{\mathrm{bad}} = 1 - f_{\mathrm{good}}$) of N data points emerging from a bad distribution with the same mean but with a different covariance matrix ($\boldsymbol{\Sigma}_{\mathrm{bad}}$). This forms our parent model with the posterior,

$$\begin{aligned} &\ln p(\bar{\mathbf{y}}, \boldsymbol{\Sigma}, f_{\mathrm{good}} | \hat{\mathbf{y}}) \\ &\propto \sum_{j=1}^{N} \log\text{−sum} - \exp(\ln f_{\mathrm{good}} \\ &+ w_j [\ln p(\hat{\mathbf{y}}_\mathbf{j} | \bar{\mathbf{y}}, \boldsymbol{\Sigma} + \mathbf{E_j}) - \ln \hat{f}_j], \\ &\ln(1 - f_{\mathrm{good}}) + \ln p(\hat{\mathbf{y}}_\mathbf{j} | \bar{\mathbf{y}}, \boldsymbol{\Sigma}_{\mathrm{bad}})). \end{aligned} \tag{5}$$

Here, j subscripts denote each galaxy, $\mathbf{E_j}$ is the observational error matrix, $\hat{f}_j$ is the normalization factor that accounts for the selection cuts in $\boldsymbol{s}$ and $\boldsymbol{m}^*$. Following the definition of the selection function, S_j, from Magoulas et al. (2012), $w_j \equiv 1/S_j$ is the inverse weighting similar to $1/V_{\mathrm{max}}$ (Schmidt 1968) that is commonly used to account for the magnitude and redshift limit of the selected sample. Strictly, the $1/V_{\mathrm{max}}$ formalism depends on the nontrivial assumptions of uniform distribution in space, no evolution across the redshift interval, and no subsets/outliers missed entirely. We note, however, that our GAMA sample is very nearly mass limited, and so our $1/V_{\mathrm{max}}$ corrections are small: only 2% of our sample have $w > 1$, with a maximum value of 2.5. The expression log-sum-exp refers to the log-sum of exponentials, which is $\ln(a + b) = \ln[\exp(\ln a) + \exp(\ln b)] = \log\text{−sum} - \exp(\ln a, \ln b)$, providing a computational convenience for sampling. Note that good, and $\boldsymbol{\Sigma}_{\mathrm{bad}}$ are declared as free parameters, with $\boldsymbol{\Sigma}_{\mathrm{bad}}$ assumed to be diagonal. We use the software `PySTAN`, the Python interface of `STAN` (Carpenter et al. 2017), to perform Markov Chain Montes Carlo (MCMC) sampling: samples are drawn from the posterior (Equation (5)) in 4 chains with each chain consisting of 1000 draws, 500 of which are warm-up, summing up to 2000 draws after discarding the warm-ups. We apply this model to the separate samples of Q and SF galaxies independently (but see Sections 3.1 and 3.3, where we model both samples combined as a single population).

The validation and verification of this model using mock galaxy samples is provided in great detail in Appendix C.

2.2.2. Constructing Linear Distance Predictors

In Dogruel et al. (2023), an SED-independent stellar-mass proxy has been calibrated, which is denoted with $\hat{M}_\star$, using the dynamical mass estimator ($\sigma_e^2 R_e$), Sérsic index (n) and rest-frame color $(g-i)_{\mathrm{rest}}$ as a hyperplane in the form of

$$\begin{aligned} \log M_\star = \alpha_0 \log(\sigma_e^2 R_e) + \alpha_1 \log \sigma_e + \alpha_2 \log n \\ + \alpha_3 (g-i)_{\mathrm{rest}} + \alpha_4. \end{aligned} \tag{6}$$

This can be readjusted using

$$\frac{M_\star}{L} L \propto k(n) \sigma_e^2 R_e \,, \tag{7}$$

where $k(n)$ is the structure correction factor as a function of Sérsic index (Bertin et al. 2002; Cappellari et al. 2006).

[13] Strictly, one should use the redshifts as observed, i.e., geocentric, not heliocentric. The difference depends on decl., latitude, and time of observation, but is at most 30 km s^{-1}, i.e., small.

Dividing both sides of Equation (7) by R_e^2 gives

$$R_e \propto k(n)\sigma_e^2\left(\frac{M_\star}{L}\right)^{-1}\left(\frac{L}{R_e^2}\right)^{-1}. \quad (8)$$

Since $\log M_\star/L_i \propto (g-i)$ (e.g., Bell et al. 2003; Zibetti et al. 2009; Taylor et al. 2011), $L/2\pi R_e^2 = \langle I_e \rangle$ and especially for $n \gtrsim 2$ as a first-order approximation, $\log k(n) \propto -\log n$, Equation (8) can be recast in log-space as

$$\log R_e = \beta_0 \log \sigma_e + \beta_1 \log\langle I_e\rangle + \beta_2 \log n + \beta_3(g-i) + \beta_4, \quad (9)$$

which can be or/or generalization of the FP, now tracking the model dependence of $k(n)$ and $M_\star/L$ through $\log n$ and the $(g-i)$ color, respectively. Henceforth, we will refer to Equation (9) as the mass hyperplane (MH).[14]

Following the same procedure in Dogruel et al. (2023), we define a subspace $\boldsymbol{Y} = (\boldsymbol{r}, \boldsymbol{s}, \boldsymbol{i}, \boldsymbol{\nu}, \boldsymbol{c})$, which is obtained from our original 8D parameter space, $\hat{\mathbf{y}}$, via the transformation $\boldsymbol{Y} = \boldsymbol{A}\hat{\mathbf{y}} + \boldsymbol{B}$. The best-fitting coefficients β_i of Equation (9) can then be calculated from the mean vector and covariance matrix $(\bar{\boldsymbol{Y}}, \boldsymbol{\Sigma_Y})$ extracted from the parent model with $\boldsymbol{\Sigma_Y} = \boldsymbol{A}\boldsymbol{\Sigma}\boldsymbol{A}^\top$ and $\bar{\boldsymbol{Y}} = \boldsymbol{A}\bar{\mathbf{y}} + \boldsymbol{B}$. Note that deriving the coefficients from $\bar{\boldsymbol{Y}}$ and $\boldsymbol{\Sigma_Y}$ is equivalent to using conditional distributions $\boldsymbol{Y_a} \mid \boldsymbol{Y_b}$ obtained by partitioning $\boldsymbol{Y}$ as $(\boldsymbol{Y_a}, \boldsymbol{Y_b})$. In this case, the slopes, $\beta_j = \partial \boldsymbol{r}/\partial \boldsymbol{x}$ for each $\boldsymbol{x} \in \boldsymbol{Y_b} = (\boldsymbol{s}, \boldsymbol{i}, \boldsymbol{\nu}, \boldsymbol{c})$, are calculated from the covariance matrices of conditional distributions $(\boldsymbol{r}, \boldsymbol{x} \mid \boldsymbol{Y_b}\backslash\{\boldsymbol{x}\})$. In Dogruel et al. (2023), the slopes derived from such conditional distributions have been referred to as isolated trends, and these characterize the variation in one parameter that can be uniquely tied to another parameter. The detailed calculations are given in Section 4.2 of Dogruel et al. (2023).

As seen in this framework, we parameterize our models by their mean vector and covariance matrices, from which we can then derive any other linear correlation as a form of post-processing. This is not just convenient but also efficient, considering that, in MCMC applications, covariance matrices have a better sampling behavior (e.g., Dam 2020) than a model parameterized with a 3D Gaussian but expressed via the plane coefficients, mean vector, and scatters (as done in Magoulas et al. 2012), particularly when the zero-point is correlated with the slopes, e.g., $c = \bar{r} - a\bar{s} - b\bar{i}$ for the FP.

2.2.3. Best-fitting Planes and Ensuing Errors in Distances

Redshift-independent distances, and thus, PVs are calculated from the offset along the r-direction, when using the FP. Magoulas et al. (2012) have shown that the distribution of galaxies about the FP in r-direction is not symmetrical when the underlying distribution is modeled with a 3D Gaussian, even though it provides a perfect empirical match. Their results imply that the plane that maximizes $p(r|s, i)$, that is, the probability density distribution of r at fixed observables s and i, does not align with the principal axes of the 3D Gaussian. In this case, the coefficients that are derived by maximizing $p(r|s, i)$ give us the direct coefficients that minimize the residuals in the r-direction, which are ideal for distance estimations as pointed out by Bernardi et al. (2003; see Appendix B).

[14] Not to be confused with the SMFP in Equation (3) or the formulation considered by Cappellari et al. (2006) and de Graaff et al. (2021), etc.

It is crucial to point out here that the direct coefficients are systematically and inescapably different (especially a) from the orthogonal coefficients that minimize the residuals perpendicular to the plane and that are derived from the eigenvector corresponding to the smallest eigenvalue of the covariance matrix, $\boldsymbol{\Sigma}_{\rm fp}$. This is because the two sets of coefficients answer two different questions. Where the orthogonal coefficients give the best description of the *true*, underlying relation within the data, the ordinary least squares (OLS) coefficients are the ones that give the best prediction (formally, the best linear unbiased estimator, or BLUE) for the true size of any given galaxy, given the data. The same argument applies to the MH in Equation (9). Within our framework, it is surely possible to fit the 5D parameter space with a hyperplane using orthogonal distance regression, though it is not straightforward to visualize, to describe the underlying distribution of the galaxy population in parameter space. Notwithstanding, direct coefficients obtained via OLS provide the answer that we want for distance estimation, by providing the BLUE values for the size, r. Therefore, we work with the direct coefficients for both the traditional FP and the MH.

Now, the issue is to calculate the intrinsic scatter in the r-direction ($\sigma_{r,\rm int}$), which will propagate through the distances and PVs. As Magoulas et al. (2012) and Said et al. (2020) have shown, orthogonal coefficients $(a_\perp, b_\perp)$ cannot yield the actual scatter in distances. In fact, for the 3D Gaussian model, when the intrinsic orthogonal scatter about the plane ($\sigma_1 = \sqrt{\lambda_1}$, where λ_1 is the smallest eigenvalue of $\boldsymbol{\Sigma}_{\rm fp}$) is projected onto the r-direction using $\sigma_{r,\rm int} = \sigma_1\sqrt{1 + a_\perp^2 + b_\perp^2}$, we heavily overestimate the scatter in distance. Throughout this work, we adopt the same approach as Dogruel et al. (2023), for calculating the errors in distances. We define a projection vector using the direct coefficients as $\boldsymbol{P} = (1, -\beta_0, -\beta_1, -\beta_2, -\beta_3)$, then the observed (total) scatter can be calculated from

$$\begin{aligned}\sigma_{r,\rm tot} &= \sqrt{\mathrm{rms}_j(\boldsymbol{P}(\boldsymbol{\Sigma_Y} + \mathbf{E_{j,Y}})\boldsymbol{P}^\top)} \\ &= \sqrt{\sigma_{r,\rm int}^2 + \sigma_{\rm err}^2}, \end{aligned} \quad (10)$$

where $\mathbf{E_{j,Y}}$ is the error matrix of the quantities in $\boldsymbol{Y}$ for the jth galaxy and $\sigma_{\rm err}$ is the scatter due to the measurement uncertainties. Equation (10) means that $\sigma_{r,\rm int} = \sqrt{\boldsymbol{P}\boldsymbol{\Sigma_Y}\boldsymbol{P}^\top}$ and $\sigma_{\rm err} = \sqrt{\mathrm{rms}_j(\sqrt{\boldsymbol{P}\mathbf{E_{j,Y}}\boldsymbol{P}^\top})}$.

3. Stellar-to-dynamical Mass Relation as a Distance Indicator

In this section, we present the properties of the MH in comparison to the FP and discuss the scatter that will propagate through the distances derived from these planes. We also demonstrate what (dis)advantages arise under different treatments of galaxy samples (combining or separating Q and SF populations). Finally, we investigate the possible sources of systematics/biases for both the FP and the MH, by studying their residual trends with several other galaxy properties.

In finding the best-fitting planar relations, we pursue an approach slightly different from what has been done before. For instance, de Graaff et al. (2021) used the FP slopes from Hyde & Bernardi (2009) that minimize the orthogonal residuals, then showed that SF galaxies lie on the same FP as the Q galaxies, but with a different zero-point and a larger scatter around the plane. In other words, the FP slopes,

naturally, have not been fitted by also including the SF galaxies in the sample. In this work, however, we calibrate the slopes of both the FP and the MH, first from the models independently applied to the separated Q and SF samples, then we repeat the procedure using the model applied to the entire galaxy sample (i.e., the combined sample of SFs and Qs, with $N = 2535$). A point worth noting here is that the astrophysical implications of this treatment for galaxy formation and evolution are beyond the scope of this paper, but clearly worth further study in a future work.

3.1. The Traditional FP

As summarized in Section 2.2.1, we can easily acquire the FP fit from our parent model via a linear transformation, which results in the model of the FP space, $\boldsymbol{x} \equiv (r, s, i)$, as a 3D Gaussian, i.e., $\boldsymbol{x} \sim \mathcal{N}(\bar{\boldsymbol{x}}, \boldsymbol{\Sigma}_{\rm fp})$.

Following Magoulas et al. (2012) and Said et al. (2020), a rough estimate for the total scatter around the FP in the r-direction can be obtained from the orthogonal coefficients through

$$\sigma^{\dagger}_{r,\rm tot} = [\epsilon_r^2 + (a_\perp \epsilon_s)^2 + (b_\perp \epsilon_i)^2 + (\sigma^{\dagger}_{r,\rm int})^2]^{1/2}, \quad (11)$$

where $\epsilon_{r,s,i}$ are the rms of the uncertainties in r, s, and i, respectively, and $\sigma^{\dagger}_{r,\rm int}$ is the intrinsic scatter in the r-direction projected from the intrinsic orthogonal scatter about the plane, as discussed in Section 2.2.3. We note that this estimate is conservative in that it assumes no unmodeled sources of error.

In Figure 3, we present the FP of GAMA galaxies in the Z band and the corresponding fit derived from the model in which the Q and SF galaxies are treated separately and independently. While the left-hand panel shows the observed effective radii plotted against the ones predicted from direct fits to the FP, the right-hand panels show the isolated trends of velocity dispersion and surface brightness. In the same way, Figure 3 shows the fit results from the model obtained when galaxies are treated together.

A more detailed look into these fit results is provided in Table 1, in which we also include the orthogonal coefficients ($a_\perp$, $b_\perp$, $c_\perp$), the conservative scatter estimates ($\sigma^{\dagger}_r$), the intrinsic orthogonal scatter about the FP (σ_1) and the rms of uncertainties (ϵ_r, ϵ_s, ϵ_i) for each FP observable, r, s, and i, respectively.

In Figure 3, we see that Q and SF galaxies in the local Universe are on the same FP, as expected from the results of Bezanson et al. (2015) and de Graaff et al. (2021). Additionally, we further verify these results in a slightly different way and show in Figure 3 that tighter FP relations can be achieved for Qs and SFs separately.

Following the arguments on the scatter of the FP by Magoulas et al. (2012) and Said et al. (2020), the true distance error is proportional to $\sqrt{(\sigma^{\dagger}_r)^2 - \sigma^2_{r,\rm int}}$. Hence, Table 1 suggests that, in principle, we might expect the PV/distance errors for our data set to be ∼0.05 dex, when the traditional FP is used. This value is similar to the estimate that can be derived from Said et al. (2020), where $\sigma^{\dagger}_r = 0.099$ and $\sigma_{r,\rm int} = 0.089$ dex; thus, the relative distance/PV errors are expected to be ∼0.04 dex.

As seen in Table 1, when the Q and SF galaxies are treated together, the scatters σ_1, $\sigma_{r,\rm int}$, $\sigma^{\dagger}_r$ are all larger than the case when Q and SF are treated separately and individually. Furthermore, it is interesting to see that under separate and individual modeling, the FP has a ∼6% smaller intrinsic scatter in the r-direction for the SF population, whereas the orthogonal intrinsic scatter about the plane seems to be the same for both populations at 0.069 dex. However, the total scatters for the SF are always larger than the ones for Q, due to SF galaxies having velocity dispersions with significantly larger uncertainties ($\epsilon_s = 0.043$ and 0.062 for Qs and SFs, respectively), while the uncertainties in both size and surface brightness are similar for both populations. Nevertheless, both populations having the same σ_1 when they are modeled independently and separately, may seem to be contradictory to de Graaff et al. (2021), who have found that the larger observed scatter seen for the SFs implies a larger intrinsic scatter because SFs and Qs in their LEGA-C sample have similar uncertainties. Though, as we stated in the beginning of Section 3, it should be considered here that de Graaff et al. (2021) have used the slopes from Hyde & Bernardi (2009) obtained through fitting exclusively Q galaxies, whereas we calibrated these slopes by also including SF galaxies, an approach which historically has not been adopted in FP studies.

3.2. The MH for Q and SF Galaxies

The MH in Equation (9) derived from the stellar-to-dynamical mass ($M_\star/M_{\rm dyn}$) relation can be regarded as an enhanced FP, now accounting for physical differences between galaxies via Sérsic index (n) and rest-frame color $(g-i)_{\rm rest}$; two of the commonly used properties that separate galaxy populations into two broad classes of early/late-types or ellipticals/spirals, etc. (e.g., Blanton & Moustakas 2009; Lange et al. 2015). The natural inclusion of these common separators within the $M_\star/M_{\rm dyn}$ relation is, in fact, crucial. For example, de Graaff et al. (2021) have stated that the physical differences between galaxies are likely to dominate the observed scatter of the FP when both Q and SF galaxies are considered. Thus, the MH here may be expected to alleviate the uncertainties attributed to these differences. Obviously, the easiest way to test this expectation is to compare the scatters of the MH and FP.

In Figure 4, we show the MH of Q and SF galaxies when they are modeled separately and independently. As in Figure 3, the left-hand panel shows the comparison between the observed and predicted $\log R_e$, while the right-hand panels show the isolated trends of σ_e, $\langle I_e \rangle$, n, and $(g-i)_{\rm rest}$. We present the more detailed fitting results in Table 2.

A comparison between Figures 3 and 4 reveals that the correlations between the pairs $(\boldsymbol{r}, \boldsymbol{s})$ and $(\boldsymbol{r}, \boldsymbol{i})$ have significantly changed with the inclusion of $\boldsymbol{\nu} \equiv \log n$ and $\boldsymbol{c} \equiv (g-i)_{\rm rest}$. As explained in more detail in Dogruel et al. (2023), this is because in the case of the FP, these correlations include the contributions from the interrelations of galaxy properties, e.g., $\boldsymbol{r}-\boldsymbol{\nu}$, $\boldsymbol{s}-\boldsymbol{c}$, $\boldsymbol{i}-\boldsymbol{\nu}$.

Unsurprisingly, the Sérsic index plays quite an important role for both populations, despite its shallower slope and lower correlation with $\boldsymbol{r}$, compared to the ones of $\boldsymbol{s}$ and $\boldsymbol{i}$ with $\boldsymbol{r}$. On the other hand, $(g-i)_{\rm rest}$ does not seem to have a noteworthy role even for the SF population which covers a much wider range in color than the Q population. This suggests that the shift from luminosity and the FP to stellar mass and the MH captures a large part of the stellar population (SP) effects that are seen to be correlated with FP residuals (see, e.g., Graves & Faber 2010; Springob et al. 2012, but see also Figure 5).

As for the scatter of the plane in the r-direction, which is the main parameter of interest concerning the distance errors, it can be seen by comparing Table 2 to Table 1 that the MH reduces

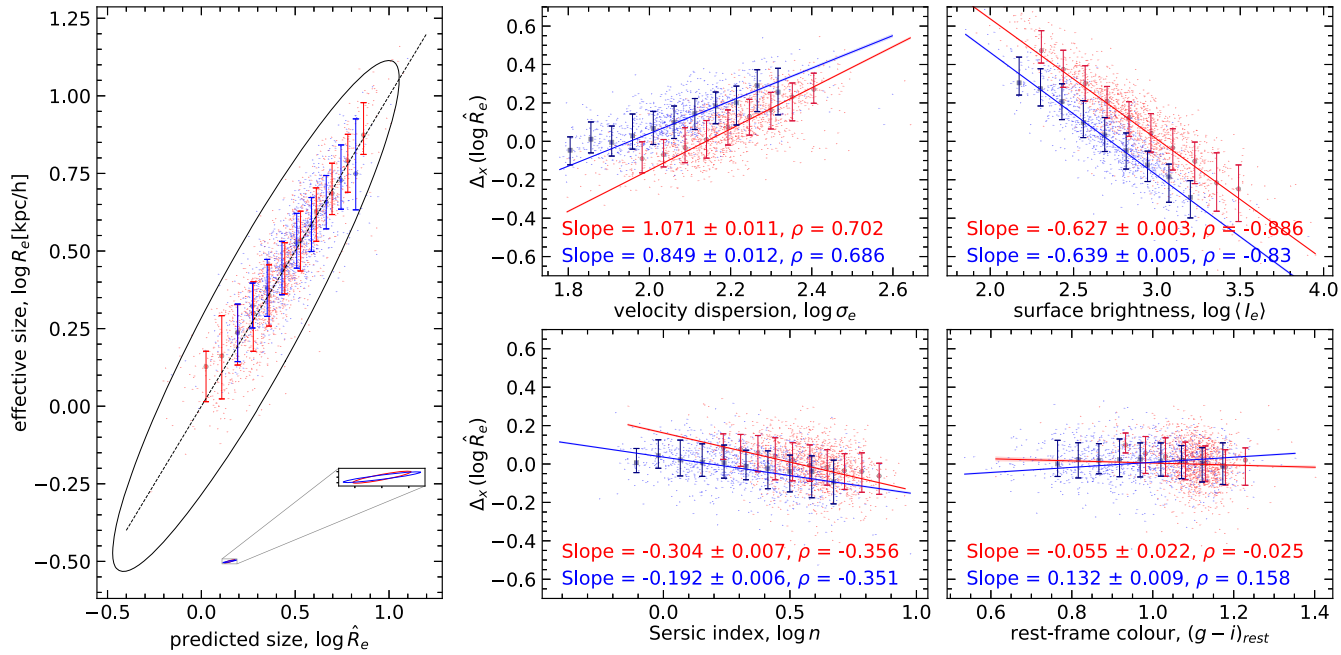

(a) Separate and independent modeling of Q and SF galaxy samples

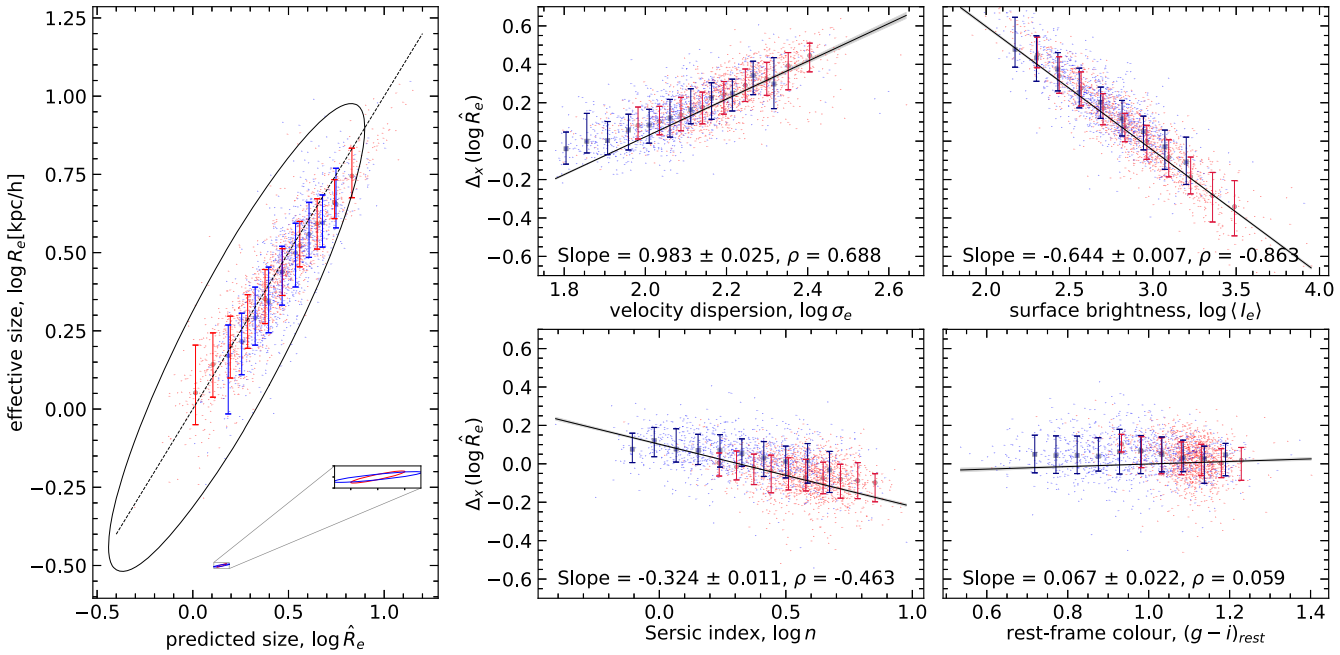

(b) Modeling the combined sample of Q and SF galaxies

Figure 3. Fit to the traditional FP of GAMA galaxies in the Z band, minimizing the residuals in the r-direction. Blue and red colors represent the SF and Q galaxies, respectively. Points show the data, while the large blue squares and red circles show the median, and the error bars show the 16/84 percentiles of the y-axis parameter in bins of the x-axis parameter. The fits are derived from our parent model applied (a) to the separate samples of SF and Q galaxies, and (b) to the combined sample. Left-hand panels: comparison of the observed effective radii to the ones predicted from the FP, along with the underlying 3σ Gaussian distribution shown with the ellipse. The zoomed-in region shows the median error ellipses. The dashed line shows the one-to-one relation. Right-hand panels: isolated trends showing the slopes of each component of the plane. Shaded regions around the lines show the 1σ uncertainty in the relevant slope. ρ in these panels represents the true correlation between R_e and the x-axis quantity, with every other quantity fixed in the parameter space. The results are normalized such that the mean value of the Δ for each sample is zero. Since the slopes are similar, the apparent offset between the two relations primarily reflects differences in the mean values of the x quantity for the two samples.

$\sigma_{r,\mathrm{int}}$ from 0.109 to 0.102 dex (∼6% decrease) for Qs and from 0.103 to 0.095 dex (∼8% decrease) for SFs. This is promising since it implies that we should be able to see an improvement in the precision of the distances from the MH by ∼6% and ∼8% for Qs and SFs, respectively, compared to the FP, when galaxy populations are modeled separately and independently.

3.3. The MH for all Galaxies

Following the seemingly promising improvement obtained with the MH in Section 3.2, we now turn our attention to fitting the MH when the combined sample of Q and SF galaxies is modeled. We present the resulting MH for this case in Figure 4,

Table 1
Properties of the FP for GAMA Galaxies in the Z Band

Parameter	Modeling the Combined Sample		Modeling Individual Samples	
	Q	SF	Q	SF
N	2535		1489	1046
a	0.676 ± 0.021		0.905 ± 0.009	0.739 ± 0.011
b	-0.654 ± 0.008		-0.598 ± 0.003	-0.645 ± 0.004
c	0.805 ± 0.042		0.158 ± 0.02	0.73 ± 0.02
$a_\perp$	0.984 ± 0.028		1.257 ± 0.012	1.02 ± 0.015
$b_\perp$	-0.74 ± 0.008		-0.599 ± 0.003	-0.755 ± 0.005
$c_\perp$	0.448 ± 0.053		-0.594 ± 0.028	0.481 ± 0.026
$\sigma_{r,\mathrm{int}}$	0.124 ± 0.002		0.109 ± 0.001	0.103 ± 0.001
ρ	0.882 ± 0.006		0.916 ± 0.002	0.848 ± 0.003
σ_1	0.085 ± 0.001		0.069 ± 0.0004	0.069 ± 0.0005
$\sigma_{r,\mathrm{tot}}$	0.127 ± 0.022	0.131 ± 0.022	0.116 ± 0.013	0.113 ± 0.014
σ_{err}	0.029	0.042	0.04	0.047
$\sigma^{\dagger}_{r,\mathrm{int}}$	0.134	0.134	0.118	0.111
$\sigma^{\dagger}_{r,\mathrm{tot}}$	0.141	0.148	0.13	0.128
ϵ_r	0.008	0.006	0.008	0.006
ϵ_s	0.043	0.062	0.043	0.062
ϵ_i	0.015	0.013	0.015	0.013

Note. Listed uncertainties correspond to 1σ confidence intervals derived from MCMC chains.

in the same fashion as Figure 3, and give further details of the MH parameters in Table 2. At first sight, these results show that the isolated trends are similar to the case of separate and individual treatment. However, as seen for the FP in Section 3.1, when the combined galaxy sample is treated as one single population, both intrinsic and total σ_r slightly increase while the correlation between observed and predicted $\boldsymbol{r}$ slightly decreases. This is expected because the inclusion of SF galaxies that have larger uncertainties in $\boldsymbol{s}$ (at least in our sample) will naturally introduce more scatter to the plane. Nevertheless, the value we get when fitting the MH for all galaxies is still just 0.11 dex, as compared to 0.124 dex for the FP for Q galaxies only. That is, the limiting precision for MH-derived distances is ∼10% better for MH relative to the traditional FP, but with the significant advantage of much larger sample sizes through the inclusion of SF galaxies (see Section 4.4 for further discussion).

3.4. Possible Systematics

In the preceding two Sections, 3.2 and 3.3, we have shown quantitatively how the MH is a tighter linear relation that is potentially capable of providing redshift-independent distances with slightly improved precision compared to the FP. In this section, we investigate whether this improvement comes with any biases and/or systematic issues.

To do this, we adopt the same approach as Dogruel et al. (2023) and analyze the residuals of both the MH and the FP as a function of several galaxy properties:

(i) Projected axis ratio, $q = b/a$,
(ii) Hα and Hδ line equivalent widths,
(iii) 4000 Å break strength, D_n4000,
(iv) Dust attenuation, $E(B-V)$,
(v) Specific star formation rate, $\mathrm{sSFR} = \mathrm{SFR}/M_\star$,
(vi) Luminosity-weighted mean stellar age, $\log\langle t_\star\rangle_{\mathrm{lw}}$, and,
(vii) Metallicity, $\log Z_\star/Z_\odot$.

Using STAN, we model the residuals ($\Delta\boldsymbol{r} \equiv \log R_e/\hat{R}_e$) as a function of each of these properties as a 2D Gaussian, then derive the best-fitting relation from this model in the form $y = Ax + B + \mathcal{N}(0, \sigma)$ where σ is the Gaussian scatter.

Starting from the axis ratio, Figure 2 shows that the residuals have a curved trend with q, which follows the $k(q)$ correction factor empirically calibrated by van der Wel et al. (2022), just as shown in Figure 7 of Dogruel et al. (2023). This is particularly prevalent for $q < 0.5$, which if adopted as the lower limit for q will reduce the sample size by ∼600 galaxies. However, if we simply apply this correction as $\log R_{e,\mathrm{corr}} = \log[R_e/k(q)]$, the residuals flatten, as shown in the right-hand panel of Figure 2. At face value, this suggests that with the inclusion of the van der Wel et al. (2022) prescription as a q-dependent correction to account for the variations in the amount of rotation versus dispersion measured by σ, we could do away with any q selection. However, to be conservative, we continue to adopt the lower limit of $q = 0.3$, as in Howlett et al. (2022).

We summarize the results for the modeling of the combined sample in Figures 5 and 6, which show that both the FP and MH have similar trends, indicating practically the same systematics with SP parameters. If anything, the MH provides slight reductions in most of these residual correlations compared to the FP.

Furthermore, we present the results for the residuals as a function of the axis ratio and observed redshift in Figure 7, which shows that despite the $k(q)$-correction, the axis ratio has a noteworthy systematic effect on the FP, just as shown in Bernardi et al. (2020), whereas this is largely reduced in the MH. Critically, redshift is not a source of systematics for either the FP or the MH.

The results are almost identical under separate and independent modeling of Q and SF populations. We should note that the approach we have applied here is to statistically compare the residual trends of both the FP and the MH, notwithstanding the astrophysical interpretation of these trends is reserved for a future work.

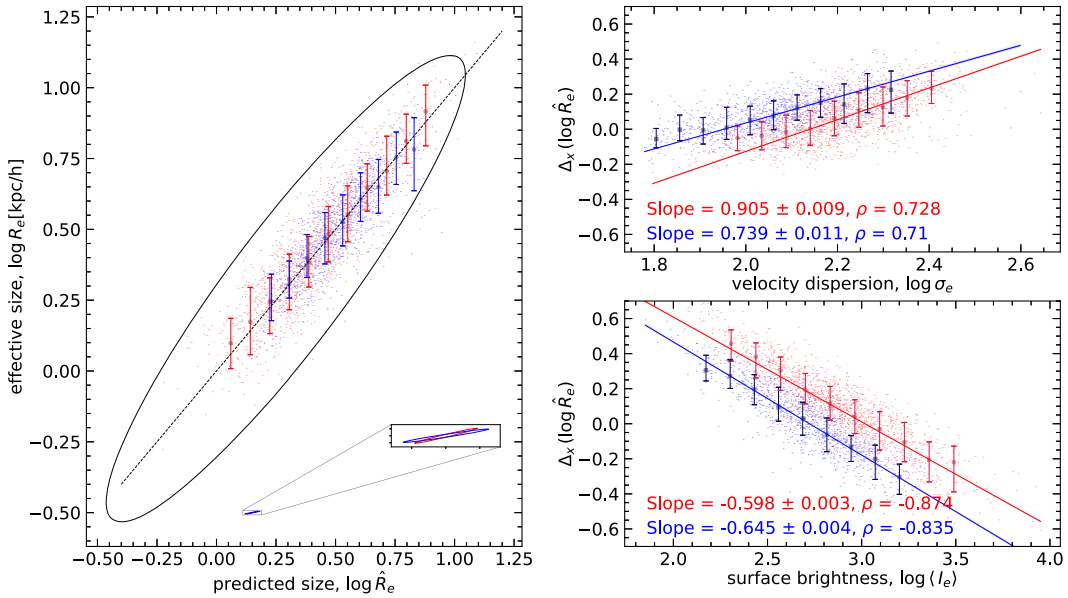

(a) Separate and independent modeling of Q and SF galaxy samples

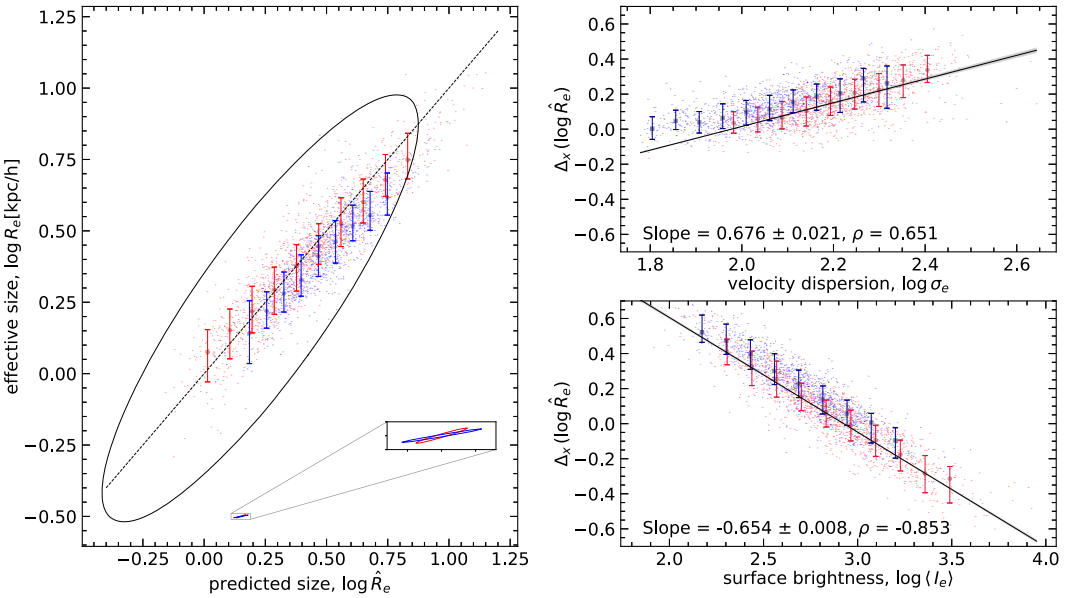

(b) Modeling the combined sample of Q and SF galaxies

Figure 4. Same as Figure 3 but for the MH.

4. PVs

4.1. Distance Ratios

For calculating the PVs, we adopt the same approach as Springob et al. (2014) and Howlett et al. (2022), where we calculate the posterior probability distributions for the distances of each galaxy. We convert the observed effective angular radii (θ_e) to physical effective radii (R_e) with $R_e = D_A(z)\theta_e$, where $D_A(z)$ is the angular diameter distance at the observed redshift (z), which may not be the same as the unknown true cosmological redshift (i.e., Hubble redshift, z_H), due to the peculiar motions of galaxies. In this case, the observed effective radii, $r_z \equiv \log[D_A(z)\theta_e]$, will be different from the true intrinsic effective radii, $r_H \equiv \log[D_A(z_H)\theta_e]$. Therefore, the offset between them is the log-distance ratios: $r_z - r_H = \log[D_A(z)/D_A(z_H)] = \log[D_C(z)/D_C(z_H)] \equiv \eta$ (see Howlett et al. 2022, footnote 4 for a detailed explanation) from which we will derive the PVs. We use the estimator to convert η to $V_{\rm pec}$ given by Watkins & Feldman (2015),

$$V_{\rm pec} \approx \frac{cz_{\rm mod}}{1 + z_{\rm mod}} \eta \ln(10), \tag{12}$$

$$z_{\rm mod} = z[1 + 0.5(1 - q_0)z - (1/6)(j_0 - q_0 - 3q_0^2 + 1)z^2], \tag{13}$$

where q_0 is the deceleration parameter and j_0 is the jerk parameter; i.e., the first and second linear derivatives of the cosmic expansion history, $H(z)$. For ΛCDM cosmology, $q_0 = -0.535$ and $j_0 = 1$. Finally, we can also calculate the cosmological distance modulus ($\mu_{\rm H}$) using the log-distance

Table 2
Properties of the MH in the Z Band

Parameter	Modeling the Combined Sample		Modeling Individual Samples	
	Q	SF	Q	SF
β_0	0.983 ± 0.025		1.071 ± 0.011	0.849 ± 0.012
β_1	-0.644 ± 0.007		-0.627 ± 0.003	-0.639 ± 0.005
β_2	-0.324 ± 0.011		-0.304 ± 0.007	-0.192 ± 0.006
β_3	0.067 ± 0.022		-0.055 ± 0.022	0.132 ± 0.009
β_4	0.205 ± 0.046		0.113 ± 0.022	0.411 ± 0.023
ρ	0.895 ± 0.004		0.927 ± 0.002	0.873 ± 0.003
$\sigma_{r,\mathrm{int}}$	0.11 ± 0.002		0.102 ± 0.001	0.095 ± 0.001
$\sigma_{r,\mathrm{tot}}$	0.118 ± 0.02	0.126 ± 0.021	0.112 ± 0.012	0.109 ± 0.014
σ_{err}	0.042	0.061	0.047	0.054

Note. Properties regarding the orthogonal fits (orthogonal coefficients, σ_1, $\sigma^{\dagger}_{r,\mathrm{int}}$, and $\sigma^{\dagger}_{r,\mathrm{tot}}$) are omitted.

ratios as follows:

$$\mu_{\mathrm{H}} = 5\log D_L(z) - 5\eta + 25 \equiv \mu_z - 5\eta, \tag{14}$$

where $D_L(z)$ is the luminosity distance in units of h^{-1} Mpc, calculated from the observed redshift, thus $\mu_z = 5\log D_L(z) + 25$. For our calculations here, we use the redshift in the CMB frame (z_{CMB}).

Our goal is to calculate the posterior probability distribution for the log-distance ratio η for each galaxy, given the data and the best-fitting MH (Equation (9)): $p(\eta_j \mid \boldsymbol{Y}_j, \overline{\boldsymbol{Y}}, \boldsymbol{C}_j^Y)$. Changing variables from $\boldsymbol{Y}$ to $\boldsymbol{Y_H} = (\boldsymbol{r_z} - \boldsymbol{\eta}, \boldsymbol{s}, \boldsymbol{i}, \boldsymbol{\nu}, \boldsymbol{c})^{\top} = (\boldsymbol{r_H}, \boldsymbol{s}, \boldsymbol{i}, \boldsymbol{\nu}, \boldsymbol{c})^{\top}$ results in $d\boldsymbol{Y_H}_j/d\boldsymbol{Y}_j = 1$. Thus, using Bayes' theorem gives

$$p(\eta_j \mid \boldsymbol{Y}_j, \overline{\boldsymbol{Y}}, \boldsymbol{C}_j^Y) = \frac{p(\boldsymbol{Y_H}_j \mid \eta_j, \overline{\boldsymbol{Y}}, \boldsymbol{C}_j^Y)p(\eta_j)}{p(\boldsymbol{Y}_j \mid \overline{\boldsymbol{Y}}, \boldsymbol{C}_j^Y)}, \tag{15}$$

where $p(\eta_j)$ is the prior. Following Howlett et al. (2022), we assume a flat prior (the natural choice given the approximately normal probability density functions (PDFs) for r and $\log D$) and generate 1000 values for η_j, uniformly distributed in the range of $[-1, 1]$ for each individual galaxy, j. This means that each galaxy will have a posterior distribution estimated at $N_\eta = 1000$ different possible distances.

Since our model is a 5D Gaussian, we would expect the posterior for each galaxy in Equation (15) to have a normal distribution as well. However, due to selection effects, the posterior will be a (slightly) skewed Gaussian rather than a perfect one (Springob et al. 2014; Howlett et al. 2022). Thus, before fitting the posteriors, the selection effects must be corrected by normalizing each posterior by

$$f_j = \int_{Y_{\mathrm{cut}}}^{\infty} p(\eta_j \mid \boldsymbol{Y}_j, \overline{\boldsymbol{Y}}, \boldsymbol{C}_j^Y) d^5\boldsymbol{Y}_j, \tag{16}$$

where Y_{cut} represents the limits stemming from our sample selection criteria. f_j will weight each galaxy to each possible distance that the galaxy could be at, so that it accounts for the galaxies missing from our sample due to our imposed selection criteria. We show how we tackle this issue in the next subsection, 4.2.

As in Howlett et al. (2022; and similar to Springob et al. 2014), we fit the normalized posteriors for each individual galaxy with a skewed normal distribution described by location (ξ_j), scale (ω_j) and shape (α_j):

$$p(\eta_j \mid \boldsymbol{Y}_j, \overline{\boldsymbol{Y}}, \boldsymbol{C}_j^Y) = \frac{1}{\omega_j}\sqrt{\frac{2}{\pi}} \exp\left[-\frac{(\eta_j - \xi_j)^2}{2\omega_j^2}\right] \times \Phi\left(\alpha_j \frac{\eta_j - \xi_j}{w_j}\right), \tag{17}$$

where Φ is the cumulative distribution function (CDF) of the standard normal distribution. It can be seen from Equation (17) that $\alpha_j = 0$ corresponds to normal distribution. In Figure 8, we show the example PDFs of five randomly chosen Q galaxies in our GAMA sample and their corresponding skew-normal fits. We calculate the parameters of interest, $\langle\eta_j\rangle$ and its standard deviation σ_{η_j} from the fitted parameters ξ_j, ω_j, and α_j, using

$$\langle\eta_j\rangle = \xi_j + \omega_j\delta_j\sqrt{\frac{2}{\pi}}, \quad \sigma_{\eta_j} = \omega_j\sqrt{1 - \frac{2\delta_j^2}{\pi}}, \quad \text{where } \delta_j = \frac{\alpha_j}{\sqrt{1+\alpha_j^2}}. \tag{18}$$

We give the distributions of $\langle\eta_j\rangle$, σ_{η_j}, and α_j in Figure 9, which shows that the shape parameter α_j is consistently nonzero for most of the galaxies, albeit small. Lastly, we should point out that PV measurements of 2496 galaxies have been obtained with this procedure after discarding the fits that have not converged.

4.2. Correction for Malmquist Bias

Due to the magnitude limit, more and more fainter galaxies will be excluded from a flux-limited sample with increasing distances. This is known as the (homogeneous, or the second type) Malmquist bias, and it affects every galaxy regardless of its position on the sky (e.g., Springob et al. 2014).

Even though we have already accounted for the magnitude and redshift limits on our sample using $w_j = 1/S_j$ in our parent Gaussian mixture model given in Equation (5), each galaxy is now being inspected at varying distances, which in turn causes varying completeness levels. Therefore, we must account for the selection effects for each individual galaxy again, but this time, we do not have to worry about $1/S_j$ weighting because, as stated in Howlett et al. (2022), it is fixed for each galaxy. The issue here is that our sample is stellar-mass limited, not flux/

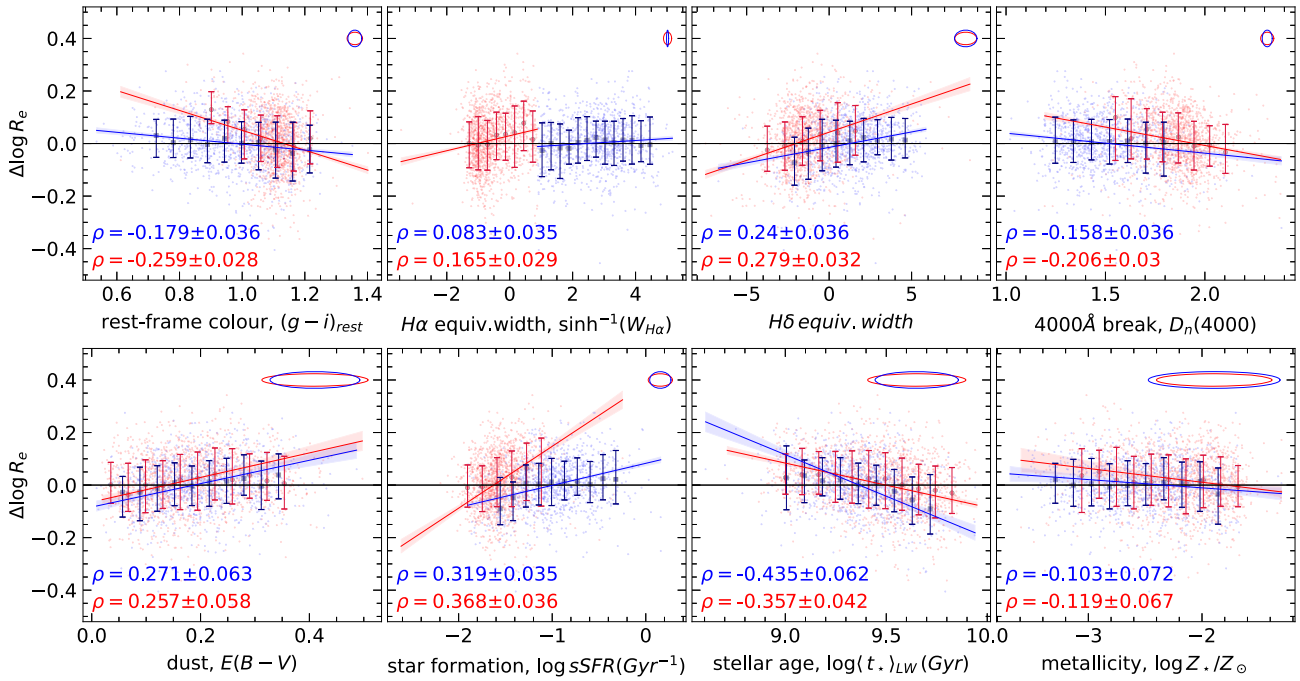

(a) Separate and independent modeling of Q and SF populations

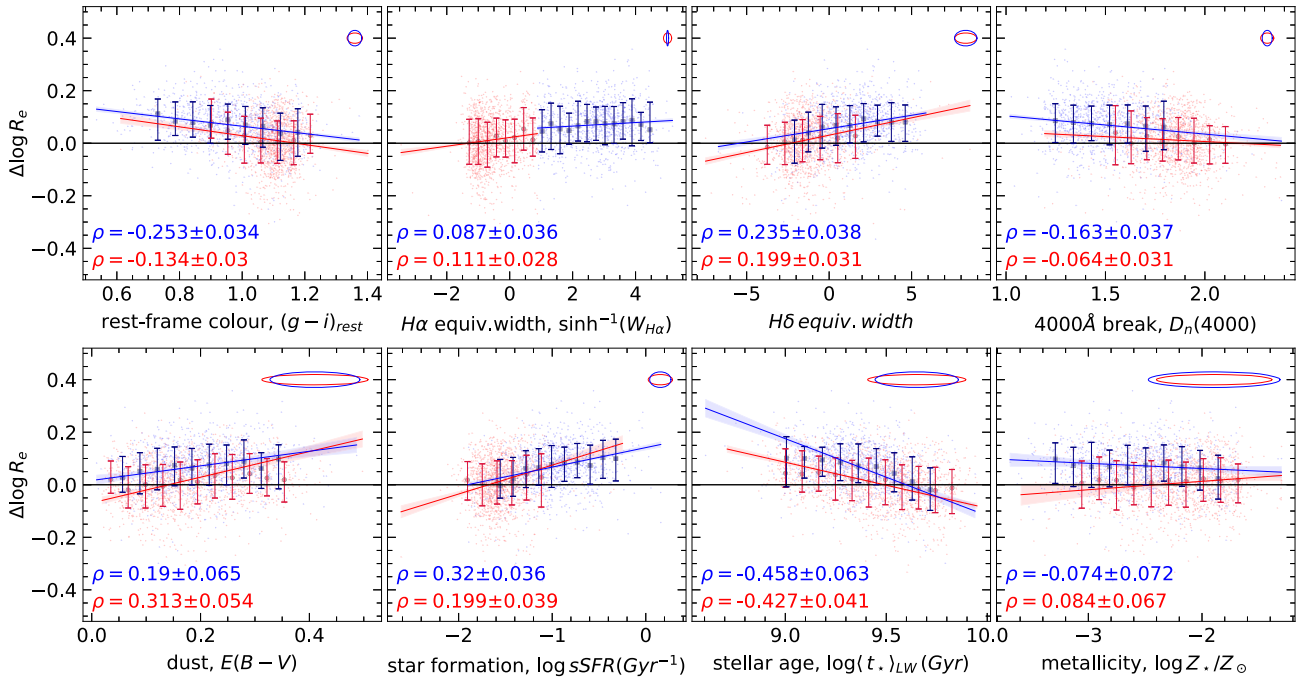

(b) Modeling the combined sample of Q and SF populations

Figure 5. FP residuals in the r-direction as a function of rest-frame color, spectral indices (Hα, Hδ, and D_n4000) and SP parameters $E(B-V)$, $\log sSFR$, $\log\langle t_\star\rangle_{LW}$, and $\log Z_\star/Z_\odot$ for (a) when Q and SF populations are modeled separately and independently, and (b) when the combined sample of Q and SF is modeled. The first row of each figure contains direct observables, and the second row contains ancillary SP parameters derived through SED-fitting. Symbols and colors are the same as in Figure 3. In each panel, smooth lines show the best-fitting line derived from the 2D Gaussian model, shaded regions around the lines correspond to 1σ uncertainty in the fit, ellipses on the upper right corner represent the median uncertainties of the data, and correlations are denoted with ρ.

magnitude limited, which changes the aspect on how the Malmquist bias applies.

Some past studies have used samples like 6dFGS and SDSS, which have been selected primarily by imposing an apparent magnitude limit. Therefore, they preferentially select intrinsically brighter galaxies at greater distances. Assuming all else being equal, this results in solutions with $\eta < 0$ (i.e., distances less than implied by the observed redshift and thus $V_{\rm pec} < 0$) being preferentially selected, which is the manifestation of the Malmquist bias in the PVs. The correction for the Malmquist bias for an apparent magnitude-limited sample is obtained through averaging over all plausible values of the galaxy

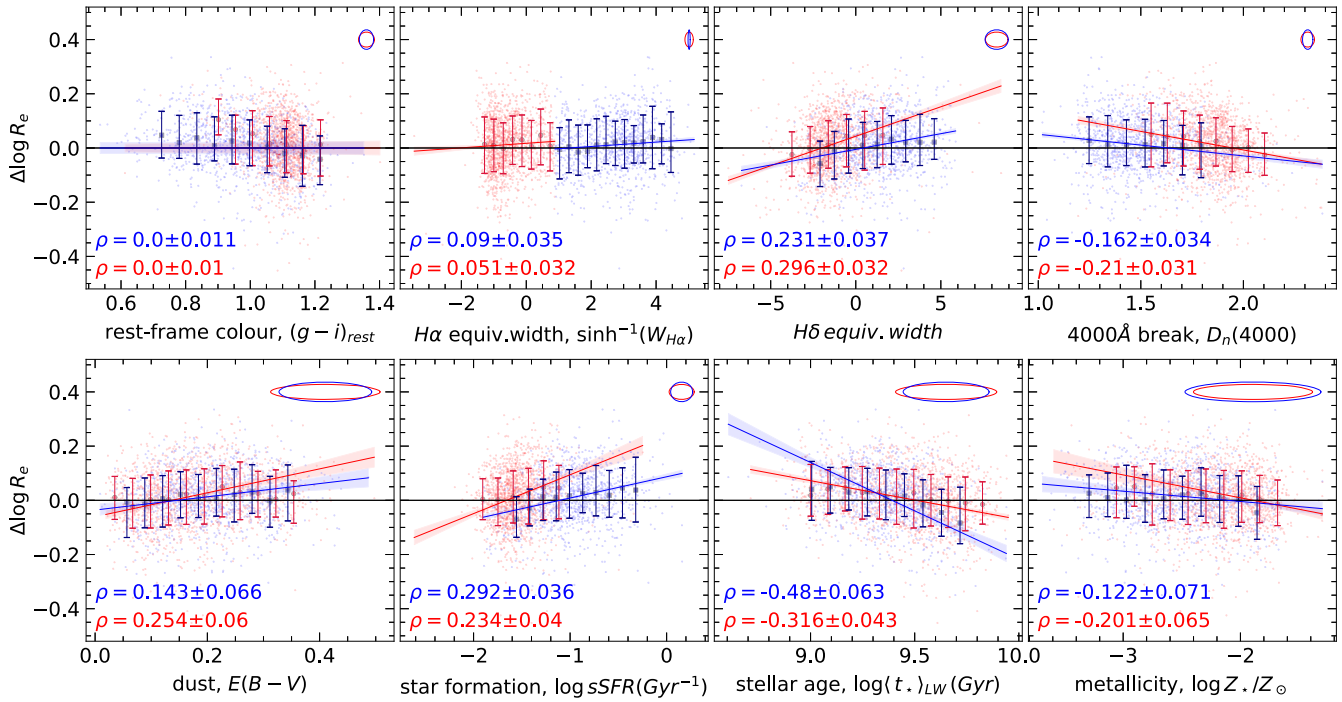

(a) Separate and independent modeling of Q and SF populations

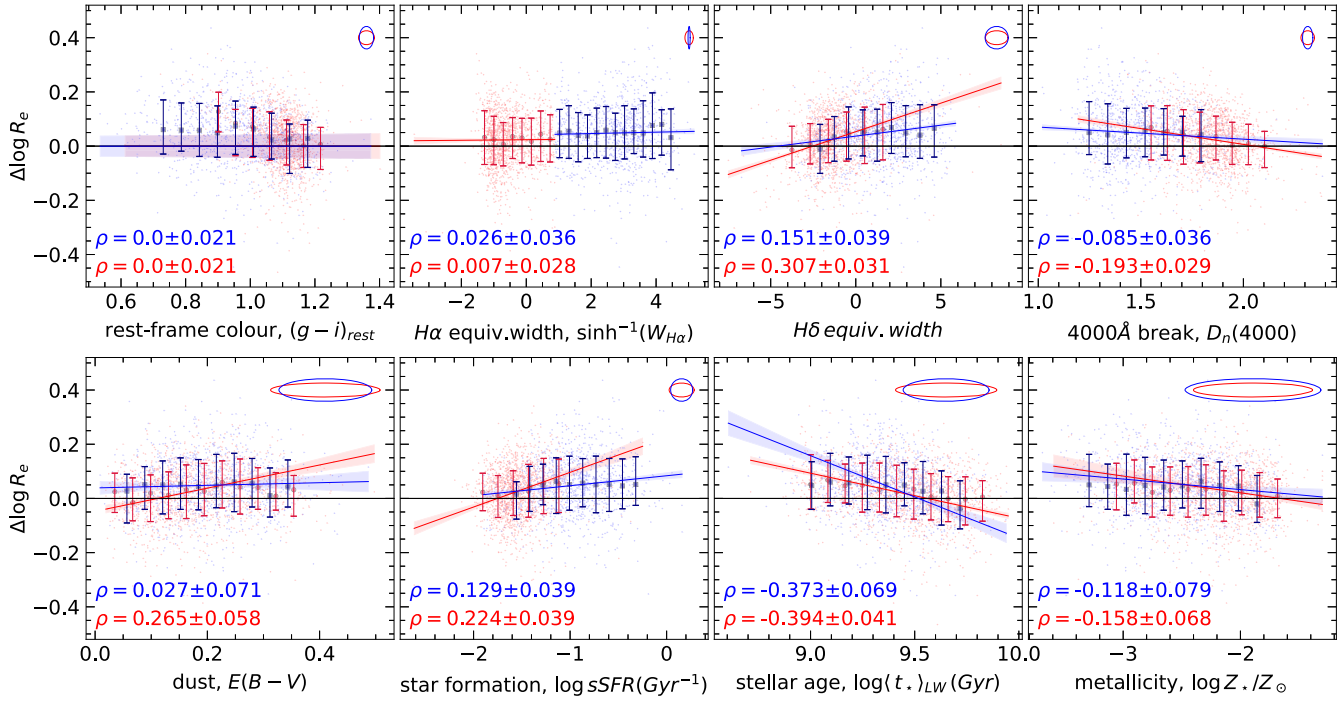

(b) Modeling the combined sample of Q and SF populations

Figure 6. Same as Figure 5 but for MH residuals in the $r-$ direction.

observables (given the data) that still satisfy the apparent magnitude selection. The usual way to do this is to determine the limiting absolute magnitude, as a function of distance, for which a given galaxy would still be included in the sample. This defines the limits of integration for the correction factor.

However, because our sample is stellar-mass limited, it is necessary to revise this correction scheme slightly, even though the basic idea remains the same. This time, the correction factor is obtained by averaging over all plausible values of galaxy observables that satisfy the mass selection condition.

Figure 10 shows the distribution of GAMA galaxies in the r-band absolute magnitude, M_r, as a function of log-luminosity distance, $\log D_L$, in the left-hand panel and as a function of stellar mass, $\log M_\star$, in the right-hand panel. Because mass and

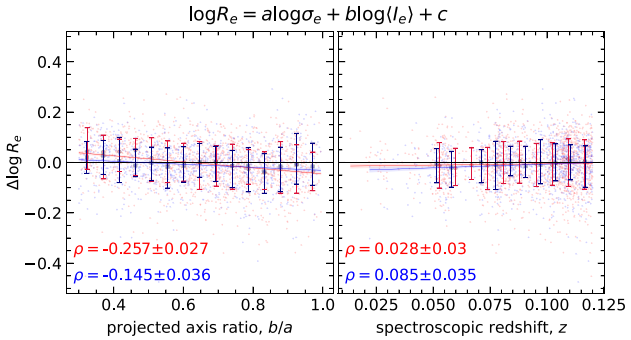

(a) For the fundamental plane

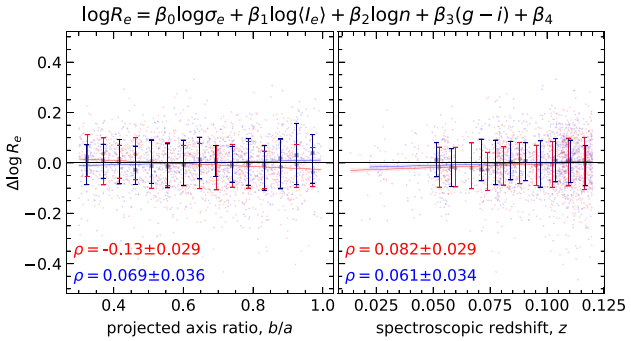

(b) For the mass hyperplane

Figure 7. Same as Figure 5 but for the residuals in the r-direction as a function of axis ratio and spectroscopic redshift.

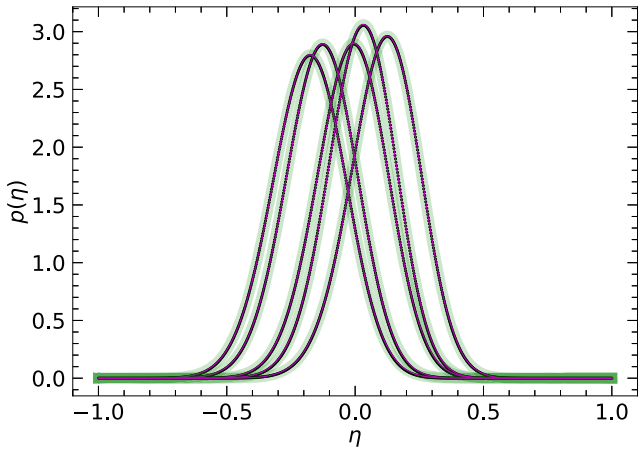

Figure 8. Normalized PDFs of log-distance ratios for five randomly chosen Q galaxies in our GAMA sample. Filled black circles show the probability distribution, and the shaded green curves show the skew-normal fits.

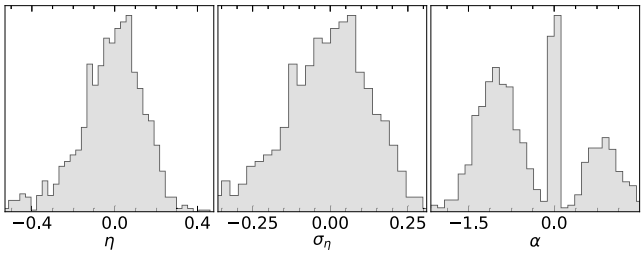

Figure 9. Distributions of the mean, standard deviation, and shape values obtained from the skew-normal fits to the PDFs of log-distance ratios for Q galaxies.

luminosity are directly correlated, it is natural to expect that a lower mass limit would cause a lower limit in absolute magnitude, $M_{r,\mathrm{lim}}$, which will be the integration limit.

The question is now to find to what distance a galaxy could still remain in the stellar-mass-limited sample if its distance were changed, which means that we need to find $M^{j}_{r,\mathrm{lim}}$ corresponding to $M_{\star,\mathrm{cut}}$. This can be done for each galaxy, j, via

$$M^{j}_{r,\mathrm{lim}} = -2.5\log\left[M_{\star,\mathrm{cut}} - \left(\frac{M_\star}{L_r}\right)_j\right] + M_{r,\odot}\,, \tag{19}$$

where the stellar mass-to-light ratio, $M_\star/L$, is measured from the SED and $M_{r,\odot}$ is the absolute magnitude of the Sun in the r band. The resulting $M_{r,\mathrm{lim}}$ is shown with red crosses on the right-hand panel of Figure 10.

However, $M_{\star,\mathrm{cut}}$ does not create a single, distance-independent $M_{r,\mathrm{lim}}$ value (see the right panel of Figure 10), as opposed to what one might expect at first sight when looking at the left-hand panel of Figure 10. Instead, as Equation (19) shows, due to the $M_\star/L$ varying for each galaxy, the fixed stellar-mass cut produces a range in limiting absolute magnitude. Moreover, the trend in $M_\star/L$ with $M_\star$, as seen in the right-hand panel of Figure 10, leads to a corresponding trend in $M_{r,\mathrm{lim}}$ with $M_\star$ as shown in red crosses. Therefore, more massive galaxies have fainter $M_{r,\mathrm{lim}}$ due to their larger $M_\star/L$ ratios. Close to the $M_{\star,\mathrm{cut}}$, the $M_{r,\mathrm{lim}}$ are close to the actual M_r; this is not a coincidence, but rather a consequence of choosing the sample stellar-mass limit to correspond to the sample apparent magnitude limit at the sample's redshift limit, as seen in the left-hand panel of Figure 10.

We now turn our attention to finding the integration limits caused by the Malmquist bias. As in Dam (2020), using $(L/L_\odot)_\lambda = 2\pi(R^{\mathrm{pc}}_{e,\lambda})^2\langle I_e\rangle_\lambda$, we find $i \equiv \log\langle I_e\rangle_\lambda = \log(L/L_\odot)_\lambda - 2(r+3) - \log 2\pi$, which leads to $i + 2r = -0.4(M_\lambda - M_{\lambda,\odot} + 2.5\log 2\pi) - 6$, where the absolute magnitudes in band λ are $M_\lambda - M_{\lambda,\odot} = -2.5\log(L/L_\odot)_\lambda$. Considering that the distance modulus is $\mu_z \equiv m_\lambda - M_\lambda = 5\log D_L[\mathrm{pc}] - 5$, we can encapsulate the constants with $\mathcal{M}_0 = 2.5\log 2\pi - M_{\lambda,\odot} + 15$ and we obtain an expression for the apparent magnitude,

$$m_\lambda = -2.5(i + 2r) + \mu_z - \mathcal{M}_0. \tag{20}$$

As stated in Springob et al. (2014) and Dam (2020), Equation (20) shows that a magnitude limit corresponds to a diagonal cut in ($\boldsymbol{r}$, $\boldsymbol{s}$, $\boldsymbol{i}$) space since magnitude is a function of both i and r. On the other hand, Equation (20) shows that a limit in absolute magnitude can also be expressed as a function of $i + 2r$, with $M_{\lambda,\mathrm{lim}} = -2.5(i + 2r) - \mathcal{M}_0$. Therefore, $M_{\lambda,\mathrm{lim}}$, which is caused by the lower limit on $M_\star$, will also result in a cut in both $\boldsymbol{r}$ and $\boldsymbol{i}$.

Even though both r and i are functions of Sérsic index n, our sample still covers the full possible range of Sérsic indices ($0.3 \leqslant n \leqslant 10$), which means that the absolute magnitude limit does not cause a cut in n. A similar result can be reached for $(g-i)_{\mathrm{rest}}$. Therefore, we only need to account for the cutoffs in $\boldsymbol{r}$, $\boldsymbol{s}$, and $\boldsymbol{i}$ in the 5D parameter space of the MH.

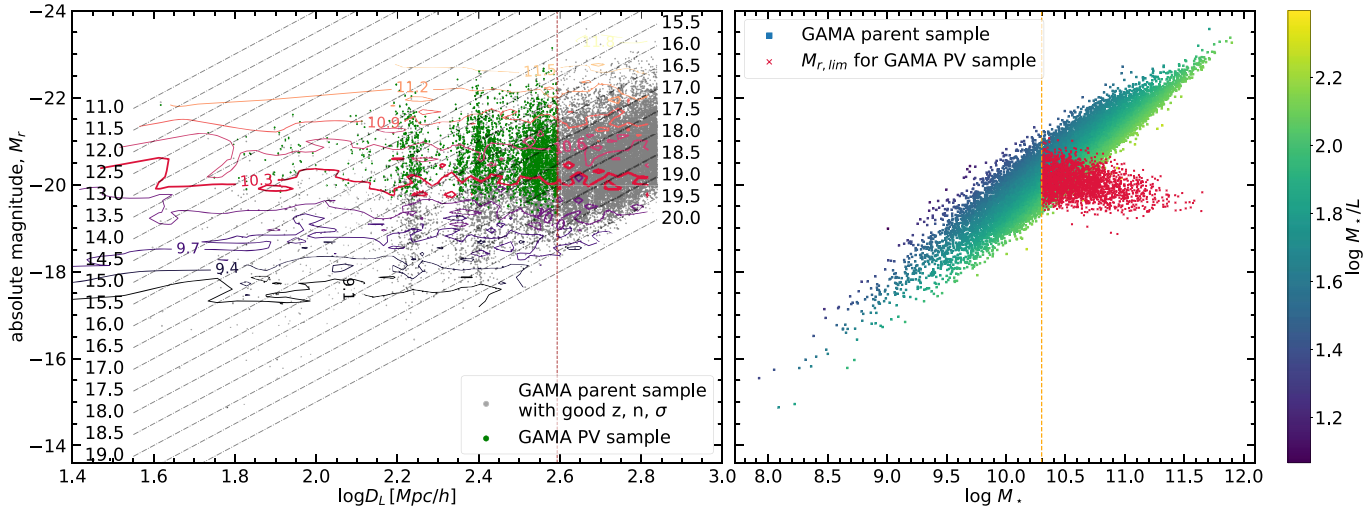

Figure 10. Left: demonstration of how Malmquist bias affects our sample in the M_r vs. $\log D_L$ plot. The gray dots represent the entire GAMA sample with reliable redshift, Sérsic index, and velocity dispersion measurements, whereas the green dots represent our adopted PV sample. Contours of $M_\star$ are also given, where the thick red contour represents $\log M_{\star,\mathrm{cut}} = 10.3$, the lower mass limit. Dash-dotted gray lines denote the Malmquist biases corresponding to the r-band limiting magnitudes given in the labels. The dashed vertical line denotes the redshift limit of our sample, $z = 0.12$. Right: M_r plotted against the stellar mass and color coded with the stellar mass-to-light ratio. Red crosses denote the limiting absolute magnitudes, $M_{r,\mathrm{lim}}$, for each galaxy in our sample, and the orange dashed line denotes the lower mass limit.

Following Dam (2020), we change variables from $\boldsymbol{Y} = (\boldsymbol{r}, \boldsymbol{s}, \boldsymbol{i}, \boldsymbol{\nu}, \boldsymbol{c})^\top$ to $\boldsymbol{w} = (\boldsymbol{u}, \boldsymbol{s}, \boldsymbol{i}, \boldsymbol{\nu}, \boldsymbol{c})^\top = (\boldsymbol{i} + 2\boldsymbol{r}, \boldsymbol{s}, \boldsymbol{i}, \boldsymbol{\nu}, \boldsymbol{c})^\top$ by

$$\boldsymbol{W} = \boldsymbol{J}\boldsymbol{Y} = \begin{pmatrix} 2 & 0 & 1 & 0 & 0 \\ 0 & 1 & 0 & 0 & 0 \\ 0 & 0 & 1 & 0 & 0 \\ 0 & 0 & 0 & 1 & 0 \\ 0 & 0 & 0 & 0 & 1 \end{pmatrix} \begin{pmatrix} \boldsymbol{r} \\ \boldsymbol{s} \\ \boldsymbol{i} \\ \boldsymbol{\nu} \\ \boldsymbol{c} \end{pmatrix} = \begin{pmatrix} 2\boldsymbol{r} + \boldsymbol{i} \\ \boldsymbol{s} \\ \boldsymbol{i} \\ \boldsymbol{\nu} \\ \boldsymbol{c} \end{pmatrix}, \tag{21}$$

where $\boldsymbol{J}$ is the Jacobian of the transformation $\boldsymbol{u} = \boldsymbol{i} + 2\boldsymbol{r}$. For a random variable having an M-dimensional normal distribution $Y \sim \mathcal{N}(\overline{\boldsymbol{Y}}, \boldsymbol{\Sigma_Y})$, the transformed variable $w = AY + B$, where $A \in \mathbb{R}^{M\times M}$ and $B \in \mathbb{R}^M$, also has an M-dimensional normal distribution with mean $\overline{w} = A\overline{Y} + B$ and covariance matrix $\boldsymbol{\Sigma_w} = A\boldsymbol{\Sigma_Y}A^\top$. Thus, Equation (16) becomes

$$f_j = \int_{\boldsymbol{w}_{\mathrm{cut}}}^{\infty} p(\boldsymbol{w}_j|\bar{\boldsymbol{w}}, \mathbf{C}_j^w) d^5\boldsymbol{w}_j, \tag{22}$$

where $\bar{\boldsymbol{w}} = \boldsymbol{J}\overline{\boldsymbol{Y}} = (\bar{i} + 2\bar{r}, \bar{s}, \bar{i}, \bar{\nu}, \bar{c})^\top$ and $\mathbf{C}_j^w = \boldsymbol{J}\mathbf{C}_j^Y\boldsymbol{J}^\top$. With this transformation, the apparent or absolute magnitude limit now corresponds to a cut in the new variable $\boldsymbol{u}$, leading to two orthogonal cuts in the $(\boldsymbol{u}, \boldsymbol{s}, \boldsymbol{i}, \boldsymbol{\nu}, \boldsymbol{c})^\top$ space: $\boldsymbol{w}_{\mathrm{cut}} = (u_{\mathrm{cut}}, s_{\mathrm{cut}}, -\infty, -\infty, -\infty)$. From Equation (20),

$$u_{\mathrm{cut}\,j,k} = -0.4(m^j_{r,\mathrm{lim}} - \mu^{j,k}_{\mathrm{H}} + \mathcal{M}_0), \tag{23}$$

where the limiting apparent magnitude for each galaxy can be calculated from Equation (19) as $m^j_{r,\mathrm{lim}} = \mu_z - M^j_{r,\mathrm{lim}}$. Notice that the cutoff u_{cut} varies not only with each galaxy but also with the distance assumed for each galaxy (Equation (14)), thus $j = 1, 2, \ldots, N$ and $k = 1, 2, \ldots, N_\eta$.

We provide the details of how to reduce Equation (22) to a simpler form as a combination of PDF and CDF of normal distribution (ϕ and Φ, respectively) in Appendix D. Since these functions are built-in and optimized in `PySTAN` (and some other computational packages), they are fast to compute. This is crucial considering that numerical evaluation of Equation (22) for large data sets is not feasible. We should also emphasize that this approach enables us to reach an exact solution instead of an approximation.

4.3. Zero-point Calibration and Comparison to the Previous Works

The zero-points in the FP and the MH expressions (Equations (1) and (9)) are c and β_4, respectively. These are obtained using the fitted slopes and means. Thus, determination of zero-points depends on the choice of which variable to minimize: residuals in the r-direction or residuals in the direction perpendicular to the plane.

In the previous works of Magoulas et al. (2012), Springob et al. (2014), Said et al. (2020), and Howlett et al. (2022), the FP has been fitted with a maximum likelihood Gaussian algorithm that models the underlying distribution as a 3D Gaussian, and thus, coefficients that minimize the orthogonal residuals have been derived. This has a key underlying assumption that the average radial peculiar velocity of the galaxies in the FP sample is zero. This is most likely not true in reality; therefore, it needs to be corrected. Said et al. (2020) have fitted the FP and the velocity field simultaneously in a Bayesian framework, eliminating the possible need for this correction. However, as stated in the beginning of this section, we use the approach of deriving PVs after fitting the FP and the MH. Thus, we need to take the zero-point considerations into account.

We calibrate our zero-point by comparing the log-distance ratios that we calculated here (for the sample of Q galaxies) to the ones from SDSS (Howlett et al. 2022) that are also included in `CF4` (Kourkchi et al. 2020). We found 268 galaxies in common after crossmatching and found the weighted mean difference in η between SDSS and our sample to be $\langle \eta_{\mathrm{SDSS}} - \eta_{\mathrm{GAMA}} \rangle = 0.068 \pm 0.01$. This value includes the uncertainty in the zero-point of `CF4` that Howlett et al. (2022) found by crossmatching their SDSS sample with `Cosmicflows-3` (Tully et al. 2016) data (0.004 dex), their uncertainty in $\bar{r}$ (0.016 dex) and finally the uncertainty in $\bar{r}$ in our study, which is derived from our ensemble of mocks

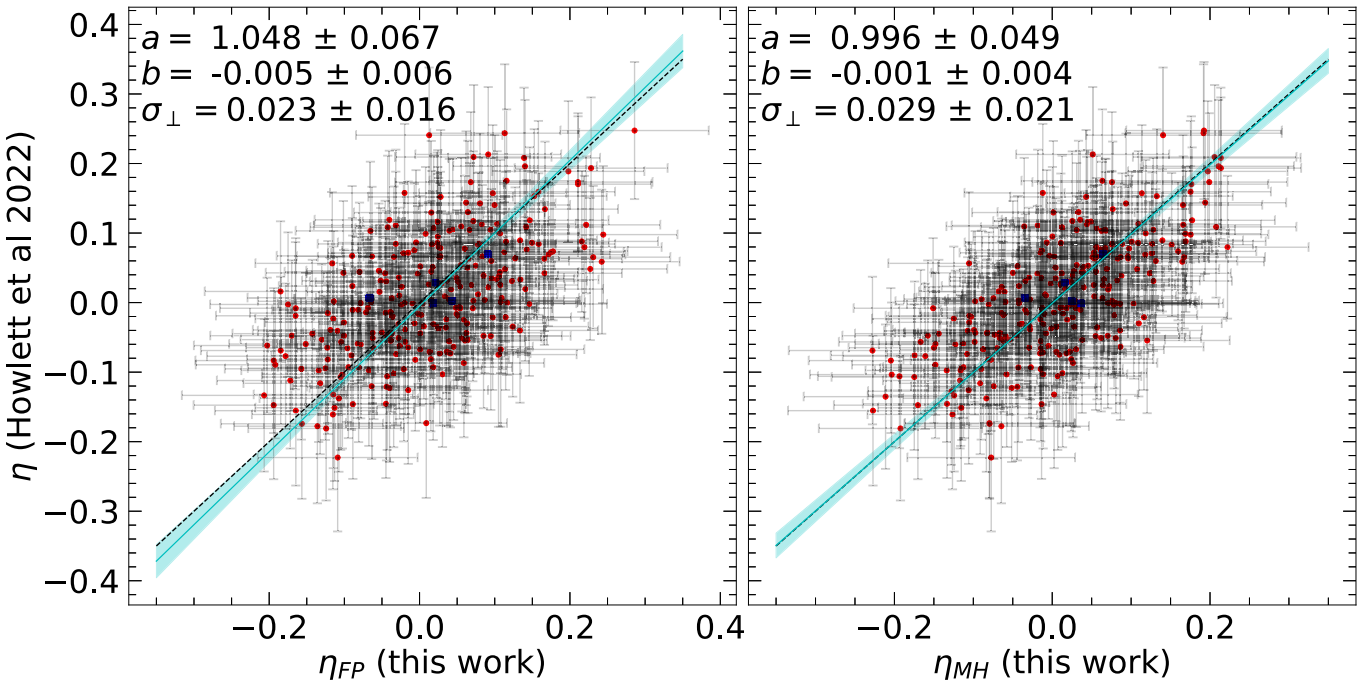

Figure 11. Comparison of our measurements of log-distance ratios, made from the FP (left) and from the MH (right) of the combined sample of Qs and SFs, to the ones of Howlett et al. (2022), for the overlapping sample of GAMA and SDSS, which consists of 268 Q galaxies in common, shown as red circles. Blue squares show the five SF galaxies found in common with CF4. In each panel, the turquoise line shows the orthogonal distance regression fit to this sample, while the shaded region around it shows the 1σ standard deviation of the fit. Slope a, intercept b and orthogonal scatter $\sigma_\perp$ from the ODR fit are given in the upper left corner. Black dashed line shows the one-to-one relation. Note that this fit is performed, excluding the three SF galaxies, after the zero-point calibration.

(Figure 18) to be 0.014 dex. Quadratic subtraction of these three contributions gives us the uncertainty in our zero-point (β_4) to be 0.064 dex. One final remark here is that Howlett et al. (2022) noted that their overlapping sample was dominated by low-redshift objects with $z < 0.05$, whereas our sample that overlaps with theirs is dominated with $z > 0.05$.

After the zero-point correction, we use ODR to fit the relation between $\eta_{\rm SDSS}$ and $\eta_{\rm GAMA}$, in the form of $y = ax + b + \mathcal{N}(0, \sigma)$, accounting for measurement uncertainties in both.[15] Figure 11 shows the comparison between these independent measurements for the overlapping sample of 268 Q galaxies. As seen here, the fit result is consistent with a one-to-one relation, verifying the apparent good agreement between these different data sets and methods. Additionally, this agreement is, in fact, so good that it does not require any correction to the slope.

We then perform a T-test (including the uncertainties in variables) between our measurements, $\eta_{\rm gama,FP}$ and $\eta_{\rm gama,MH}$, and the ones from Howlett et al. (2022), $\eta_{\rm sdss}$, to further test the consistency of our measurements. We find that the T-statistic and the p-value to be $t = -0.007$, $p = 0.994$, and $t = -0.005$, $p = 0.996$ for the pairs of $\eta_{\rm SDSS} - \eta_{\rm GAMA,FP}$ and $\eta_{\rm SDSS} - \eta_{\rm GAMA,MH}$, respectively. This means that the difference between $\langle\eta_{\rm SDSS}\rangle$ and $\langle\eta_{\rm GAMA}\rangle$ (through both the FP and MH) are not statistically significant.

It is straightforward to think that we can simply compare the distances for SF galaxies that we have computed in this work, to the ones from CF4 derived through the TFR, and see whether this method really works for SFs. Unfortunately, the CF4 TFR sample and our GAMA sample have only five SF galaxies in common. Even relaxing our $\log M_\star/M_\odot > 10.3$ cut raises this number to only 12. Although Figure 11 shows the consistency between the η values of these five SF galaxies for CF4 and GAMA, it is obviously nowhere near being statistically sufficient to draw any conclusions on the relation between these different estimates.

We can, however, use galaxy groups and the fact that galaxies in the same group should be at more or less the same distance. Thus, we can look at galaxy groups in our sample that have both SF and Q, then compare the distances of SF galaxies, $\log D(z_H)$, that we have derived from the log-distance ratios, to the ones of Q galaxies that are in the same galaxy group. Using the galaxy groups from Robotham et al. (2011), we find 180 groups in our sample that have at least one Q and one SF. For each group, we take the weighted mean of the $\log D(z_H)$ distances of Qs and SFs separately, and plot these in Figure 12. We then perform an ODR fit using STAN and find that the relation between the $\log D(z_H)$ distances to Qs and SFs that are in the same galaxy groups is consistent with a one-to-one relation, as seen in the left-hand panel of Figure 12. Furthermore, in the right-hand panel of Figure 12, we plot the differences between the distances of Q and SF galaxies that are in the same group against the group redshift. An OLS fit to the distribution in this figure shows that the variation of distance differences with group redshift is consistent with zero, thus, showing no signs of biases.

The fact that the MH yields distance estimates with no appreciable bias for Q versus SF galaxies in the same group, and with $\approx$0.07 dex or 16% scatter for each population, is truly remarkable. This has the potential to significantly expand future PV cosmology samples through the inclusion of all (massive) galaxies. At least as significantly, it also argues against any appreciable redshift-dependent bias that might creep in through the relative proportion of Q versus SF galaxies.

[15] This fit was performed with the SciPy.ODR package of Python.

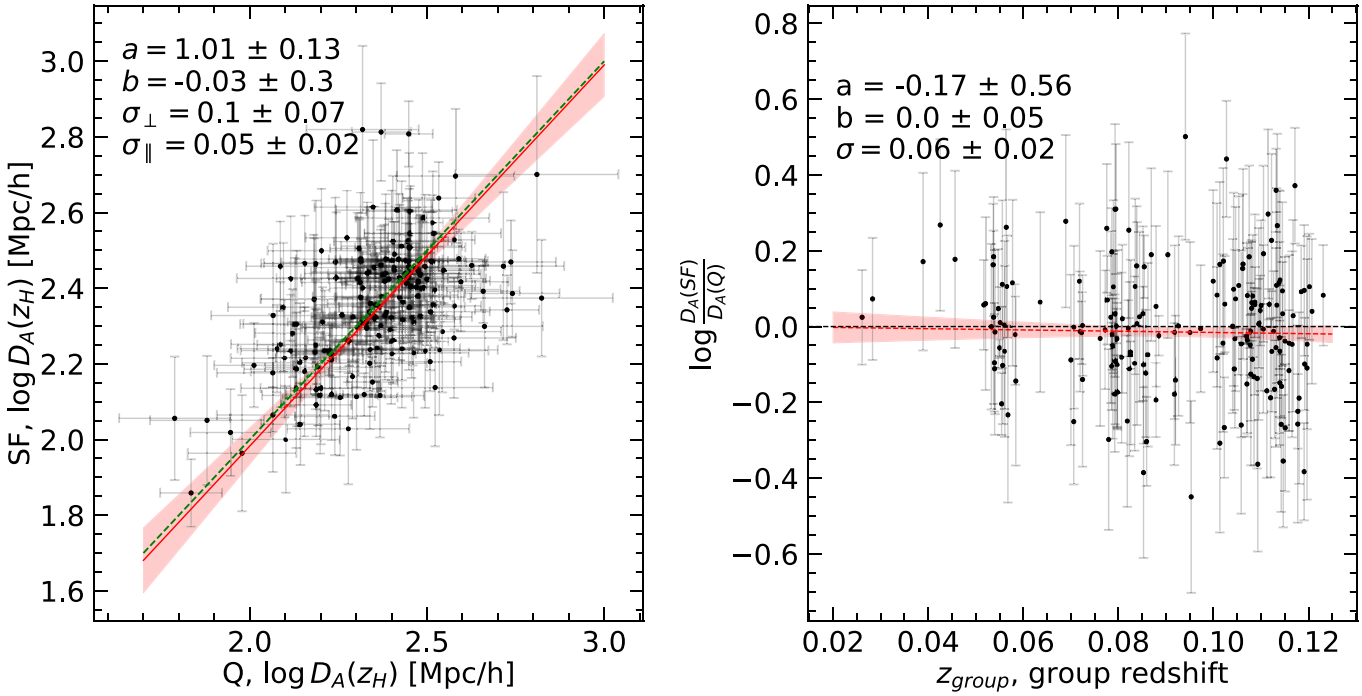

Figure 12. Comparison of the weighted means of the angular diameter distances derived from η measured through the MH for SF and Q galaxies in the same groups. Left: the dashed-green line shows the one-to-one relation, whereas the red line shows the mean relation between the Q and SF distances obtained by an ODR fit. The shaded red region around the mean line shows the 1σ uncertainty. Note that the implication is that the independent Q- and SF-derived distances for groups agree with a $\sigma_{\parallel} = \sigma_{\perp}/\sqrt{1+a^2} \approx 0.17$ dex scatter in each, and no appreciable bias. Right: the difference between Q- and SF-derived group distances, plotted as a function of group redshift. Red line shows the fit obtained through OLS, which is consistent with zero. This lack of a significant trend with group redshifts means our PV measurements do not show biases with redshift, at least across the redshift range of our sample.

4.4. Comparison to the FP: The Value of the MH for PV Cosmology

As discussed in more detail in Section 3, a comparison between Tables 1 and 2 shows that the intrinsic scatter, $\sigma_{r,\mathrm{int}}$, is smaller in the MH than in the FP, irrespective of the galaxy type and the sample used in fitting. This raises the question of whether this improvement in the tightness of the plane would manifest itself in the measurements of η. To address this question, we can simply repeat the measurements in Sections 4.1 and 4.2 for the traditional FP and measure the rms scatter of the observed η distributions for both the FP and MH.

In Figure 13, we show the distributions of η for Q galaxies as measured from the FP and the MH. We fit these with skew-normal distributions using `PySTAN`, then derive the mean ($\langle\eta\rangle$) and standard deviation (σ_{η}) values using Equation (18). While the standard deviation (which corresponds to the distance error in this case) is 0.139 ± 0.004 dex for the FP-derived distances, it is 0.136 ± 0.004 dex for the MH, which means that, in practice, the precision of the distances measured from the MH is not significantly better than with the FP. Repeating the same procedure to the SF sample, we see similar. We provide a similar discussion in Appendix E for the case of separate and independent modeling of galaxy populations. This suggests that observational errors in the measurements of galaxy properties and/or in the derivation of Malmquist bias corrections may make a substantial contribution to the final error budget for η, at least for this sample. We therefore conclude that while, in principle, the use of the MH can lead to a $\approx$10% improvement in the precision of distance estimations, in practice it may be hard to realize that potential. Even so, we have shown how our MH formalism and analysis can be applied not only to Q galaxies, but to the broader $\log M_{*} \gtrsim 10.3$ galaxy population, with an increase of 70% or greater in sample size and a commensurate increase in statistical power.

5. Summary and Conclusions

In this work, we have introduced the MH as a recasting of the $M_{\star}/M_{\mathrm{dyn}}$ relation, which provides an FP-like linear distance indicator. We have modeled both the FP and the MH for Q and SF galaxies separately, showing that both populations follow similar relations (Figures 3 and 4). Further, we have demonstrated that both populations can be modeled as a single FP or MH relation with a slightly larger intrinsic scatter. That is, the FP and the MH are not specific to a certain class of galaxies, but apply to all (field) galaxies as a population. This result broadly agrees with the growing consensus, including authors like Bezanson et al. (2015), de Graaff et al. (2020), and de Graaff et al. (2021).

As well as showing the importance of accounting for projection effects (Figure 2), we have made a thorough comparison between the MH and the FP, and explored their possible systematics by studying their residuals as a function of SP parameters (Figures 5 and 6), along with axis ratio and redshift (Figure 7). Then, we have set out to determine the redshift-independent distances of both Q and SF galaxies of GAMA at $z < 0.12$ simultaneously using the MH. We have tested the validity of our framework by comparing our distance/PV estimates made through both the FP and the MH to the previous measurements for Q galaxies from SDSS (Figure 11). To perform this test for the SF galaxies, we compare the distances to groups independently derived for Q and SF galaxies (Figure 12). Finally, we have compared

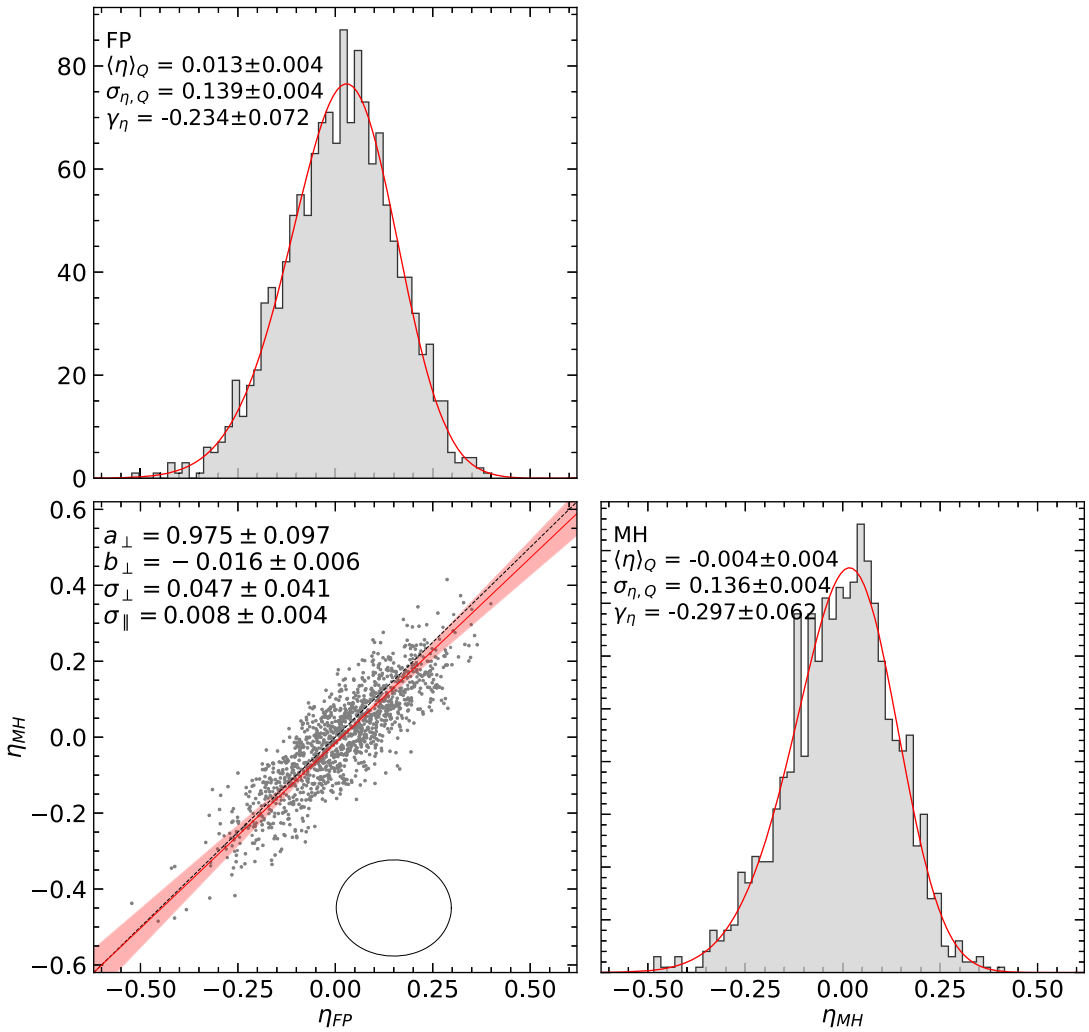

Figure 13. η measurements carried out through the FP and the MH for Q galaxies. Diagonal panels show the histograms of $\eta_{\rm FP}$ and $\eta_{\rm MH}$. Smooth red curves show the best-fitting skew-normal distributions obtained via `PySTAN` . The mean ($\langle\eta\rangle$), standard deviation (σ_η), and skewness (γ_η) are given in the upper left corner of each diagonal panel. The lower left panel gives the comparison of these measurements plotted against each other. Dashed line shows the one-to-one relation, while the red line and shade show the best-fitting linear relation and the corresponding 1σ region. Fit parameters are given in the upper left-hand corner. Finally, the mean error ellipse is shown in the lower right-hand corner.

distance/PV measurements from the FP to the ones from the MH (Figures 13 and 14).

Our results are summarized as follows:

1. Both the FP and the MH can be obtained by fitting either the individual Q and SF samples or the combined sample (Figures 3 and 4), although separate and individual fitting results in smaller intrinsic scatters in the r-direction, i.e., tighter planes for distance estimation. However, in all cases of fitting, the MH slightly reduces the intrinsic scatter compared to the FP by at least ∼6% (Tables 1 and 2), which may slightly improve the precision of the redshift-independent distance estimates.
2. The intrinsic scatter (in the r-direction, $\sigma_{r,\rm int}$) of the MH is ∼10% smaller than for the FP. Therefore, the limiting precision for MH-derived distances is ∼5%–10% better compared to the FP. While SF and Q galaxies can be described with a single FP or MH relation, obtaining separate/independent FP and MH relations result in ∼10% smaller $\sigma_{r,\rm int}$ relative to a single FP/MH fit. That is, using a Q- or SF-specific FP/MH relation gives the best precision in distance estimates (Tables 1 and 2).
3. Similar to Graves et al. (2009) and Springob et al. (2012), we have found strong correlations between stellar population properties (such as age/D_n4000, SFR) and $\Delta \log R_e$ residuals of either the FP or the MH relations (Figures 5 and 6). Further, we see similar variations with spectral and SED-derived properties ($g-i$, H_α, H_δ, D_n4000, $E(B-V)$, sSFR, and $\log\langle t_\star\rangle_{\rm lw}$, $Z_\star$ for both the FP and MH, showing that the inclusion of the rest-frame color as a SP diagnostic, provides a modest benefit. The same can be said for the inclusion of Sérsic index as a proxy for stellar/dynamical structure.
4. The projection effects seen as a function of axis ratio ($q = b/a$) are substantial. Although we have limited our analysis to $q > 0.3$, we have also shown that the empirical description of van der Wel et al. (2022) provides a good way to describe this effect (Figure 2). Future PV studies carried out via the FP/MH may either simply adopt the van der Wel et al. (2022) prescription or may be able to incorporate a similar parameterization into the model to calibrate these effects, which can possibly eliminate the need for an axis ratio selection.

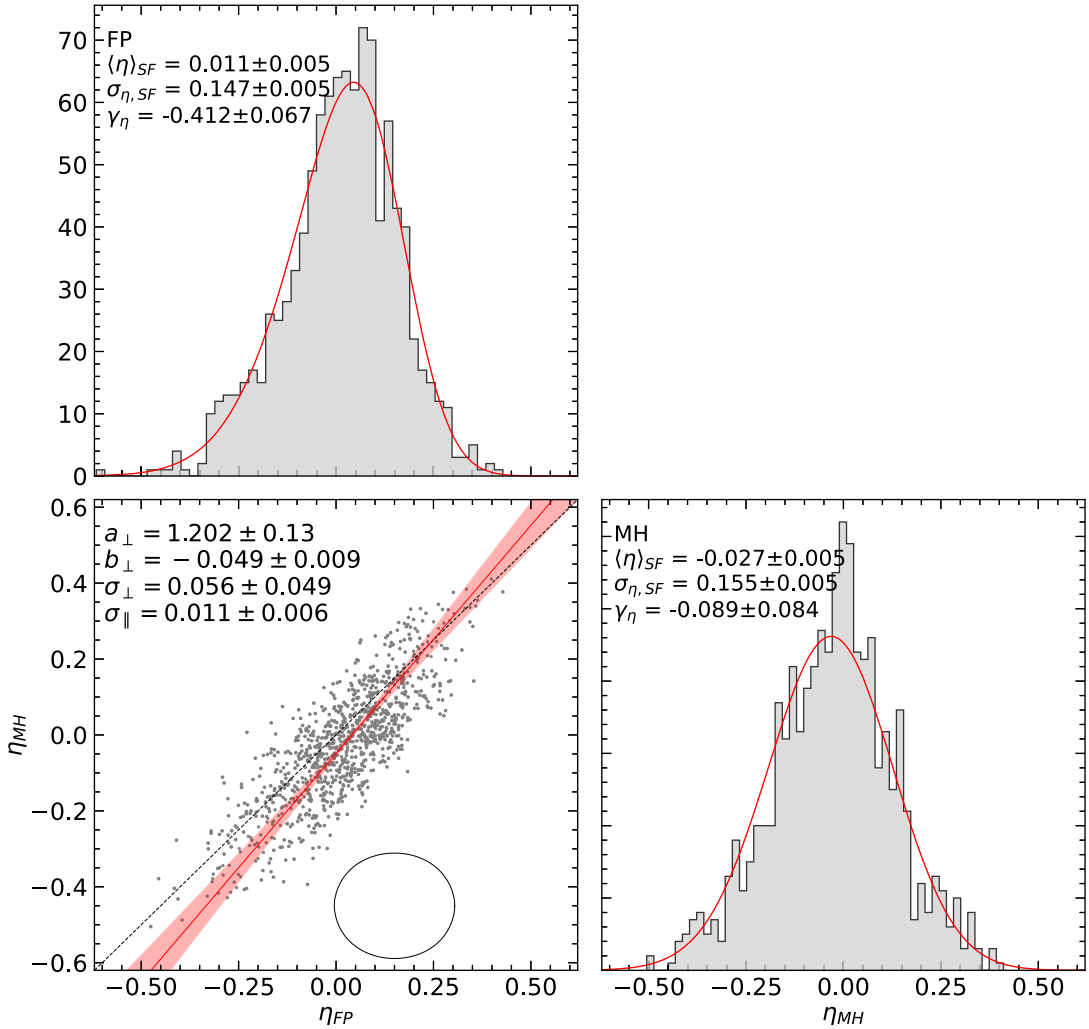

Figure 14. Same as Figure 13 but for the SF galaxies in our sample.

5. We have validated our MH framework as a tool for PV cosmology by directly comparing our MH-derived distances to the latest FP-derived distances of Q galaxies for SDSS from Howlett et al. (2022). We have found an excellent agreement with a random scatter of ∼0.1 dex (Figure 11), i.e., one-to-one agreement within measurement errors and with no discernible bias.
6. For validating our MH framework for SF galaxies, we compared the MH-derived group distances based on SF galaxies to the ones based on their Q counterparts in the same group. We have shown that both measurements are consistent with each other, with a random scatter of ∼0.1 dex, while showing no discernible bias as a function of inferred distance or group redshift (Figure 12).
7. The ∼10% improvement in the intrinsic scatter in the r-direction when the MH is used, does not seem to translate as an improvement in the precision of z-independent distance estimates, as seen in, e.g., Figure 13, which might be caused by the additional sources of observational uncertainties in the MH. This result is similar to Springob et al. (2012, 2014) who found that even though the FP residuals correlate strongly with stellar age, adding it to the FP does not provide improvement for distances. Furthermore, modeling the galaxy sample as one population may save time; however, it may result in larger uncertainties. Meanwhile, using the same form of the planar relation, albeit with different coefficients acquired by modeling the populations separately and independently, most likely constitutes the best approach (Figures 20 and 21), as it reduces the scatter in distances compared to the combined treatment of galaxy populations.

Overall, we have shown that the sample size for a PV study can be significantly increased (by $\gtrsim$70%) through the inclusion of SF galaxies in both the FP and the MH, which is particularly valuable when the data required for the TFR are not available. For example, the 4MOST Hemisphere Survey will measure the PVs for ∼650,000 early-type galaxies via the FP to map the cosmic velocity field and to measure the growth of structure in the local Universe, up to $z \sim 0.12$ (Taylor et al. 2023). In this context, the framework presented in this study can potentially improve the precision of the cosmological measurements as well as increasing the number of galaxies up to a million.

Acknowledgments

K.S. acknowledges support from the Australian Government through the Australian Research Council's Laureate Fellowship funding scheme (project FL180100168).

Appendix A
Consistent Velocity Dispersion Measurements across Heterogeneous Spectroscopic Data

Many targets in the GAMA sample have been previously observed by other spectroscopic surveys, most notably SDSS, 2dFGRS, and 6dFGS. The spectra from these surveys have been retrieved and incorporated into the GAMA database, including for the purpose of measuring redshifts, emission lines, etc. Some of these targets have been reobserved by GAMA, mostly as filler and/or low priority targets. This means that while the GAMA redshift sample is well defined and virtually complete, the spectroscopic data quality is inhomogeneous, and there are potential systematic effects across the selection boundaries of the different surveys. This appendix describes the process by which we have measured velocity dispersions from this heterogeneous spectral data set, and how we have ensured consistency across the measurements obtained from different surveys' spectra.

Our velocity dispersion measurements are derived using `pPXF` (Cappellari 2017), which forward models the observed data as a linear combination of template stellar spectra broadened with a Gaussian convolution kernel. We use the MILES stellar library (Sánchez-Blázquez et al. 2006) as our template set, adopting 2.51 Å as a consensus value for the effective spectral resolution (Falcón-Barroso et al. 2011). One important decision is the inclusion additive and multiplicative polynomials in the fits: we use a 10th-order additive Legendre polynomial and a fifth-order multiplicative Legendre polynomial. This step is strictly necessary for the 2dFGRS and 6dFGS spectra, which are not flux calibrated. As well as sidestepping potential issues in background subtraction and/or flux calibration in the spectra, the inclusion of these polynomials means that the results are constrained by the shapes of broad absorption features in the stellar continuum rather than overall continuum shape/color or the absolute/relative strengths of different spectral features.

The spectral resolution for the data is a critical input to the process, since this cannot be empirically separated from the true intrinsic broadening in the spectrum. Our assumed spectral resolutions for each survey are given in Table 3, including an independent characterization of the spectral resolution for 6dF, which is based on sky line measurements. Compared to the estimates from Jones et al. (2009), this reduces the inferred 6dF velocities dispersions by ≈5%, and is necessary to bring the 6dF-derived measurements into good agreement with other surveys. The template spectra are smoothed to match this resolution and then both templates and data are rebinned to a common log-wavelength grid before the PPXF fits.

We use a two-stage process to measure and subtract strong emission lines and isolate the stellar continuum in the observed spectra. In the first stage, spectra are fit as a combination of stellar templates plus kinematically distinct sets of both Balmer and also forbidden emission line templates. Any emission lines that are detected at $>5\sigma$ in this first stage are marked and retained; all other lines are discounted. This initial stage protects against over-fitting in the second and final stage.

The error propagation from counts on the detector to velocity dispersion measurements is not linear, and there are significant unmodeled sources of error in the measurements (including through seeing variations). Thus, some rescaling of the estimated uncertainties on the inferred velocity dispersions is justified. We use repeat observations of the same targets within each survey to calibrate the quoted errors/uncertainties, by finding the scalar value, u, required to bring the NMAD spread between repeat observations (of the same target by the same survey) to have a nominal χ^2 equal to 1. Note that for 6dFGS, we have performed this exercise for the full 6dFGS spectral database, not only the 19 6dFGS galaxies that were reobserved by GAMA. The results, shown in Figure 15, do not show significant variation as a function of measured velocity dispersion, except where the inferred values are comparable to the resolution limit of the spectra. (We have also checked this explicitly by computing the scaling factor in decile bins of the pairwise mean observed velocity dispersion and signal to noise (S/N), and see no effect.)

Next we have compared cross-survey repeats of the same targets to test for potential systematic errors across the heterogeneous data set, as shown in Figure 16. Given that observed velocity dispersion peaks in the center and decreases approximately monotonically with the projected radius, some systematic differences are to be expected across surveys due to differing fiber sizes, different median seeing, etc. To bring measurements from the different surveys to a common standard, we recalibrate each survey to match the values derived from SDSS spectra, since this is the survey with the highest spectral resolution and widest area. We fit a function of the form $f(S; a, b, c) = b \cdot \exp[-a\,(S-5)] + c$ to the cross-survey data comparisons, where S is the median S/N across the available spectrum in units per angstrom, and the values of the coefficients a, b, and c are survey specific. For 6dFGS, we find the value of the coefficient b to be statistically indistinguishable from zero, so we drop this value for the fit. Further, for GAMA, we find the values of both b and c to be consistent with 0; that is, we find no clear statistical evidence of the need for a correction, and so no correction is applied. These cross-calibrated values, which are reported in the GAMA `VelocityDispersions` DMU as `SIG_STARCORR` are what we use in this paper, and what are recommended for use where homogeneous velocity dispersion measurements are required.

In the final panel of Figure 16, we show a spectrum-by-spectrum match between 719 of the velocity dispersion measurements described here and those presented by Howlett et al. (2022), which are derived following a very similar process. Noting that this comparison is restricted to a high S/N subset of the spectra we consider here, the mean and rms difference between our measurements and those from Howlett et al. (2022) are −0.018 and 0.015 dex, respectively. The systematic difference is small, but non-negligible, and left uncorrected would induce a systematic bias in the inferred distances/velocities between our two catalogs. Similarly, the rms differences are small, but significant, considering that the two values are derived from the same high S/N measurements; they are in fact comparable in size to the median statistical uncertainty on each measurement, which is ≈0.02 dex. This shows how, for $S/N \gtrsim 15$, both the precision and the accuracy of these values are limited by the analytic methods used to derive the velocity dispersion measurements, at least as much, if not more so, than statistical measurement errors in the spectra themselves.

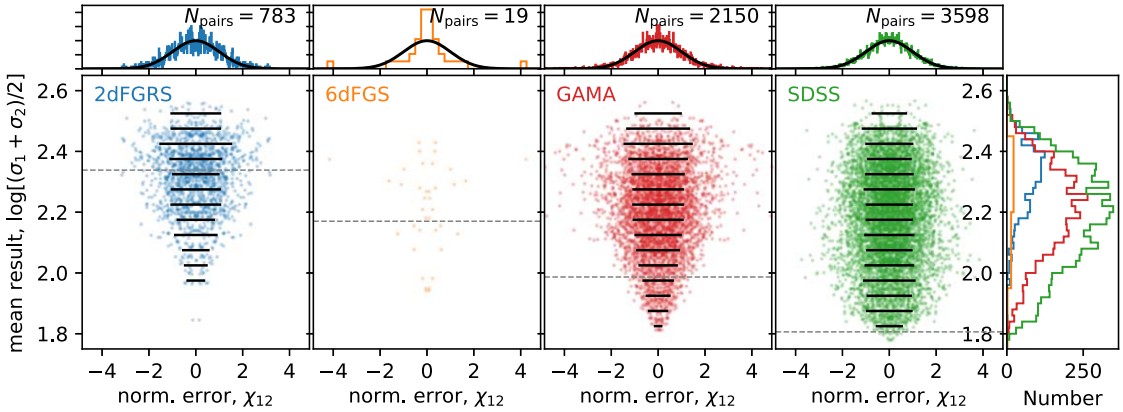

Figure 15. Intra-survey comparisons of velocity dispersion measurements from repeat observations. From left to right, we show pairwise comparisons of velocity dispersion measurements from repeat observations by 2dFGRS, 6dFGS, GAMA, and SDSS, each plotted as a function of the pairwise mean value, and normalized by the reported errors, added in quadrature. These results can be used to rescale/calibrate the reported uncertainties on the measurements from each data source.

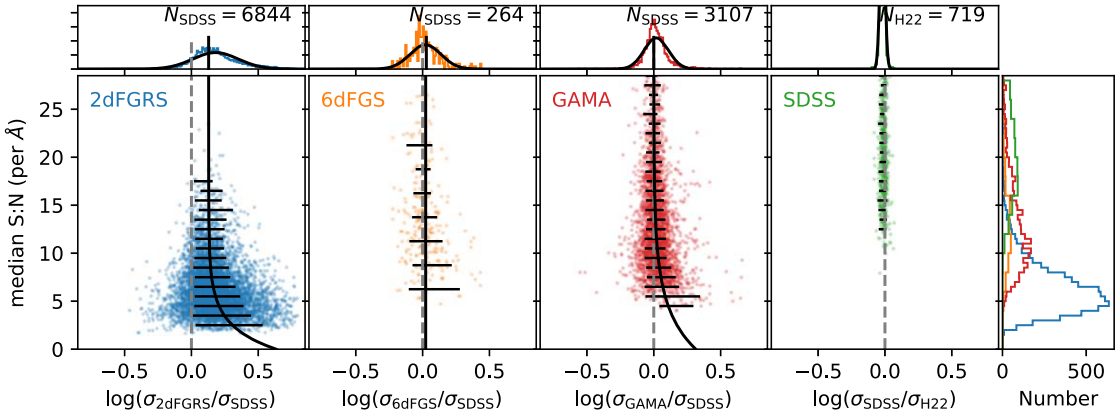

Figure 16. Left: cross-survey comparisons of velocity dispersion measurements for common targets between SDSS and other surveys. In the first three panels, we show, from left to right, pairwise comparisons of velocity dispersion measurements for common targets between SDSS and each of 2dFGRS, 6dFGS, and GAMA, each plotted as a function of median S/N in that survey. These results can be used to quantify/recalibrate bias in the measurements at low S/N, as shown by the black curves. In the final panel, we compare our measurements based on SDSS spectra to the measurements from Howlett et al. (2022), which are based on a similar (but not identical) process applied to the same spectra. This provides a means to calibrate both random and systematic errors associated with the choice of algorithm.

Table 3
Summary of Spectral Data Sources and Recalibration Parameters

Survey	λ (Å)	$\lambda R(\lambda)$ (km s^{-1})	σ_{lim}	N_{targ}	N_{meas}	u	a	b	c
(1)	(2)	(3)	(4)	(5)	(6)	(7)	(8)	(9)	(10)
2dFGRS	3546–6849	9.0	218	14720	13782	1.01	0.479	0.215	0.107
6dFGS	3772–7220	$13.764(\lambda/10^4\text{Å} + 1.1295)$	148	974	952	⋯	0.738	0	0.0035
GAMA	3772–7220	4.8 (4.5) @ 4800 (7250) Å	97	88504	85687	1.59	0	0	0
SDSS	3541–7407	from `WDISP` FITS ext.	64	26818	23122	0.93	⋯	⋯	⋯

Note. Columns: (1) name of survey; (2) median useful wavelength range (constrained by both the data and the MILES template library); (3) adopted spectral resolutions, which for 2dFGRS, GAMA, and SDSS are as described by Colless et al. (2001), Hopkins et al. (2013), and Abazajian et al. (2009), respectively; (4) effective velocity dispersion measurement limit as determined by the median spectral resolution; (5) number of velocity dispersion measurements from each survey in the catalog; (6) number of unique galaxies with velocity dispersion measurements from each survey in the catalog; (7) error rescaling factor for each survey, derived from intra-survey repeat observations as shown in Figure 15; (8–10) bias correction parameters for each survey, derived from cross-survey comparisons with SDSS as shown in Figure 16. The final catalog contains a total of 132326 independent measurements for 111831 unique targets.

Appendix B
Direct versus Orthogonal Coefficients in Distance Determination from the FP

The importance of obtaining the direct coefficients in distance determinations, instead of the orthogonal ones that define the underlying distribution, can be better understood when we algebraically find the coefficients that maximize $p(r|s, i)$ given our best-fitting model. In the 3D Gaussian case, we have $\boldsymbol{x} - \bar{\boldsymbol{x}} = (r - \bar{r}, s - \bar{s}, i - \bar{i})$ and the best-fitting model that can be easily obtained from our parent model is $\boldsymbol{x} \sim \mathcal{N}(\bar{\boldsymbol{x}}, \boldsymbol{\Sigma}_{fp})$,

which makes the log-likelihood,

$$\ln p(r|s,\, i,\, \bar{\boldsymbol{x}},\, \boldsymbol{\Sigma}_{\rm fp}) = -\frac{1}{2}(\boldsymbol{x} - \bar{\boldsymbol{x}})\boldsymbol{\Sigma}_{\rm fp}^{-1}(\boldsymbol{x} - \bar{\boldsymbol{x}})^{\top} + \text{const.} \tag{B1}$$

After expanding the matrix multiplication and considering that s and i are fixed at their observed values, this equation can be reduced to

$$\ln p(r|s,\, i,\, \bar{\boldsymbol{x}},\, \boldsymbol{\Sigma}_{\rm fp}) = \gamma_0 + \gamma_1(r - \bar{r}) + \gamma_2(r - \bar{r})^2, \tag{B2}$$

where

$$\begin{aligned} \gamma_1 &= 2[(s - \bar{s})\Lambda_{12} + (i - \bar{i})\Lambda_{13}], \\ \gamma_2 &= \Lambda_{13}, \quad \Lambda = \boldsymbol{\Sigma}_{\rm fp}^{-1}, \end{aligned} \tag{B3}$$

and γ_0 encapsulates all the constants arising during the process. We are looking for the values, r_*, that will maximize Equation (B1), in other words, $\partial \ln p/\partial r = 0$. Therefore, $2\gamma_2(r_* - \bar{r}) + \gamma_1 = 0$, which leads to

$$r_* = -\frac{\Lambda_{12}}{\Lambda_{11}}s - \frac{\Lambda_{13}}{\Lambda_{11}}i + \bar{r} + \frac{\Lambda_{12}}{\Lambda_{11}}\bar{s} + \frac{\Lambda_{13}}{\Lambda_{11}}\bar{i}. \tag{B4}$$

This is just $r_* = as + bi + c$ with $a = -\Lambda_{12}/\Lambda_{11}$, $b = -\Lambda_{13}/\Lambda_{11}$ and $c = \bar{r} - a\bar{s} - b\bar{i}$. Now, expanding $\Lambda = \boldsymbol{\Sigma}_{\rm fp}^{-1}$,

$$\begin{aligned} \Lambda_{11} &= \frac{\sigma_s^2\sigma_i^2 - \sigma_{si}^2}{|\boldsymbol{\Sigma}_{\rm fp}|}, \quad \Lambda_{12} = \frac{\sigma_{ri}\sigma_{si} - \sigma_{rs}\sigma_i^2}{|\boldsymbol{\Sigma}_{\rm fp}|}, \\ \Lambda_{13} &= \frac{\sigma_{rs}\sigma_{si} - \sigma_i^2\sigma_{ri}}{|\boldsymbol{\Sigma}_{\rm fp}|}, \end{aligned} \tag{B5}$$

which finally gives

$$a = \frac{\sigma_{ri}\sigma_{si} - \sigma_{rs}\sigma_i^2}{\sigma_{si}^2 - \sigma_s^2\sigma_i^2}, \quad b = \frac{\sigma_{rs}\sigma_{si} - \sigma_{ri}\sigma_s^2}{\sigma_{si}^2 - \sigma_s^2\sigma_i^2}. \tag{B6}$$

These are the direct coefficients given by Bernardi et al. (2003), and they minimize the residuals in the r-direction (i.e., OLS), which is what really matters for distance measurements.

Appendix C
Mock Galaxy Catalogs

We generate mock samples starting from the algorithm of Magoulas et al. (2012) to create FP parameters $(r,\, s,\, i) \equiv (\log R_e,\, \log \sigma_e,\, \log\langle I_e\rangle)$, and then we calculate other galaxy parameters using relevant scaling relations. These samples will be used in the validation of the fitting method (i.e., determination of the accuracy and precision) we describe in Section 2.2 and also in estimating the errors in the best-fit parameters, as in Magoulas et al. (2012) and Said et al. (2020).

The $v-$space comprises three orthonormal vectors $(\hat{\boldsymbol{v}_1},\, \hat{\boldsymbol{v}_2},\, \hat{\boldsymbol{v}_3})$ that define the axes of the 3D Gaussian of the FP, and they are expressed in terms of the FP slopes a and b (Colless et al. 2001; Magoulas et al. 2012). The distribution of galaxies in the FP space will, therefore, be oriented around these axes with variances σ_1, σ_2, σ_3, and the center of the 3D Gaussian will be at the mean values $(\bar{r},\, \bar{s},\, \bar{i})$ of the FP observables.

To generate other galaxy parameters, we use four scaling relations: stellar mass versus color (Taylor et al. 2015), stellar mass-to-light versus color (Taylor et al. 2011), stellar mass versus dynamical mass (Taylor et al. 2010), and size versus Sérsic index (Caon et al. 1993) each having slope (A_{XY}), intercept (B_{XY}) and intrinsic scatter (σ_{XY}). These relations have the form $Y = A_{XY}X + B_{XY} + \epsilon_{XY}$, where $\epsilon_{XY} = \mathcal{N}(0,\, \sigma_{XY})$ represents Gaussian scatter around the mean linear relation. As such, we use 20 parameters in total to generate an extensive mock galaxy catalog. The input values for these parameters are obtained from our best-fitting model to the GAMA sample defined in Section 2.

The algorithm for generating the mock samples is outlined below.

1. Calculate the v-axes using the FP slopes a and b.
2. Calculate the covariance matrix by $\boldsymbol{\Sigma}_{\rm FP} = \boldsymbol{V}\boldsymbol{\Lambda}\boldsymbol{V}^{\top}$ where $\boldsymbol{V}$ is the matrix containing $\hat{\boldsymbol{v}_1}, \hat{\boldsymbol{v}_2}, \hat{\boldsymbol{v}_3}$ as columns and $\boldsymbol{\Lambda} = \text{diag}(\sigma_1^2,\, \sigma_2^2,\, \sigma_3^2)$.
3. Draw $\{r,\, s,\, i\}$ values randomly from a 3D Gaussian with mean $(\bar{r},\, \bar{s},\, \bar{i})$ and covariance matrix $\boldsymbol{\Sigma}_{\rm FP}$
4. Distances and redshifts: Draw values randomly from a uniform distribution for comoving volume $V_{\rm com}$, derive comoving distances $D_{\rm com}$ from $V_{\rm com}$, then derive redshifts from $D_{\rm com}$. Finally, convert $D_{\rm com}$ to angular diameter distance D_A.
5. Magnitudes: Derive apparent (m_λ) and absolute magnitudes (M_λ) using surface brightness and effective radius in step 3 and distances in step 4.
6. Error estimates: Generate 2% uncertainties for i and s, calculate uncertainty in r with $\varepsilon_r = 0.5\varepsilon_i$, then generate correlated errors from these uncertainties using a correlation coefficient -0.92 between ε_r and ε_i
7. Add measurement errors in step 6 to $\{r,\, s,\, i\}$ in step 3 to obtain the observed FP parameters.
8. Calculate *selection probability* from Equation (10) of Magoulas et al. (2012) using the r-band magnitude limit of GAMA: $r_{\rm lim} = 19.8$ mag (AB units).
9. Generate Sérsic indices with $\log n = A_{\nu r}\log R_e + B_{\nu r} + \epsilon_{\nu r}$.
10. Estimate uncertainty $\epsilon \log n \equiv \epsilon_\nu$ using ϵ_r and the relevant scaling relation, then generate correlated errors using these uncertainties and correlation coefficient 0.76.
11. Add the errors to $\log n$ from step 9 to obtain observed Sérsic indices.
12. Calculate $M_{\rm dyn}$ using $k(n)$ from Bertin et al. (2002) with r and s from step 3 and Sérsic index from step 9.
13. Generate stellar-masses with $\log M_\star = A_{\rm msd}\log M_{\rm dyn} + B_{\rm msd} + \epsilon_{\rm msd}$
14. Generate color from stellar mass with $\text{color} = A_{\rm mc}\log M_\star + B_{\rm mc} + \epsilon_{\rm mc}$
15. Obtain observed values using correlated errors as in step 10 with correlation coefficient 0.5
16. Generate stellar mass-to-light ratio from rest-frame color with $\log M_\star/L = A_{\rm mlc}\,\text{color} + B_{\rm mlc} + \epsilon_{\rm mlc}$, then obtain observed values as in steps 10 and 15.
17. Luminosity can be calculated using either absolute magnitudes in step 5 or using $M_\star/L$ and $M_\star$ from steps 14–16.
18. Finally, apply selection limits discussed in Section 2.1: $0.01 < z < 0.12$ and $10.3 \leqslant \log M_\star$.

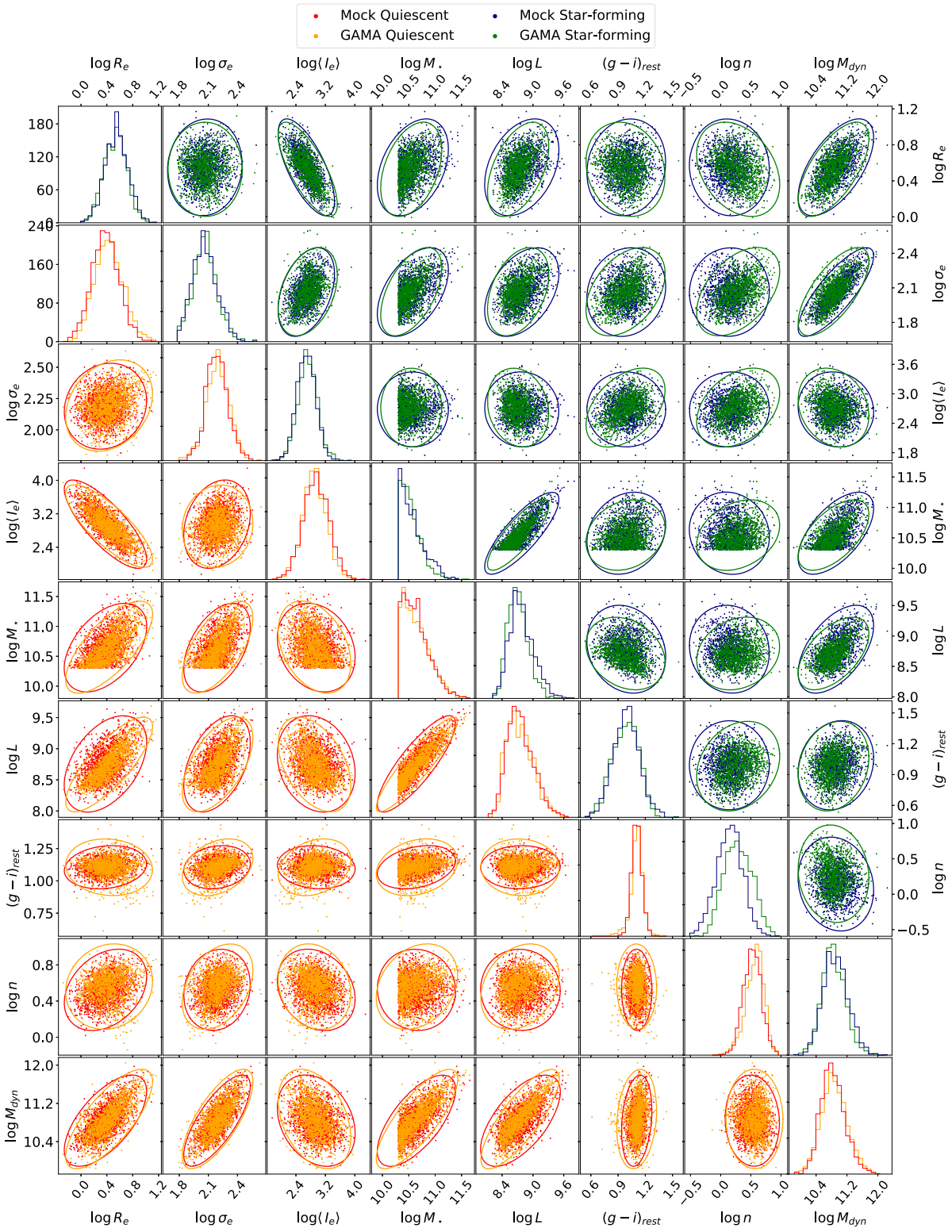

Figure 17. Illustration of mock samples for both early (lower left panels) and late-type galaxies (upper right panels) in comparison to GAMA samples overlaid with 99% confidence ellipses showing the underlying Gaussian distribution, corresponding to each sample.

The same algorithm can be applied to generate samples for SFs, using the input parameters derived from the corresponding best-fitting model to the GAMA SF sample. One of the mock samples for both Qs and SFs, together with the actual GAMA Q/SF samples is shown in Figure 17, where the close agreement between mocks and actual data can be seen.

We have validated our model by verifying our ability to robustly recover the known input parameters for many mock samples. The results of this exercise are summarized in Figure 18: each panel shows the histogram of the fitted parameter from 1000 mock samples, with the black continuous curve showing the best-fitting Gaussian to the histogram.

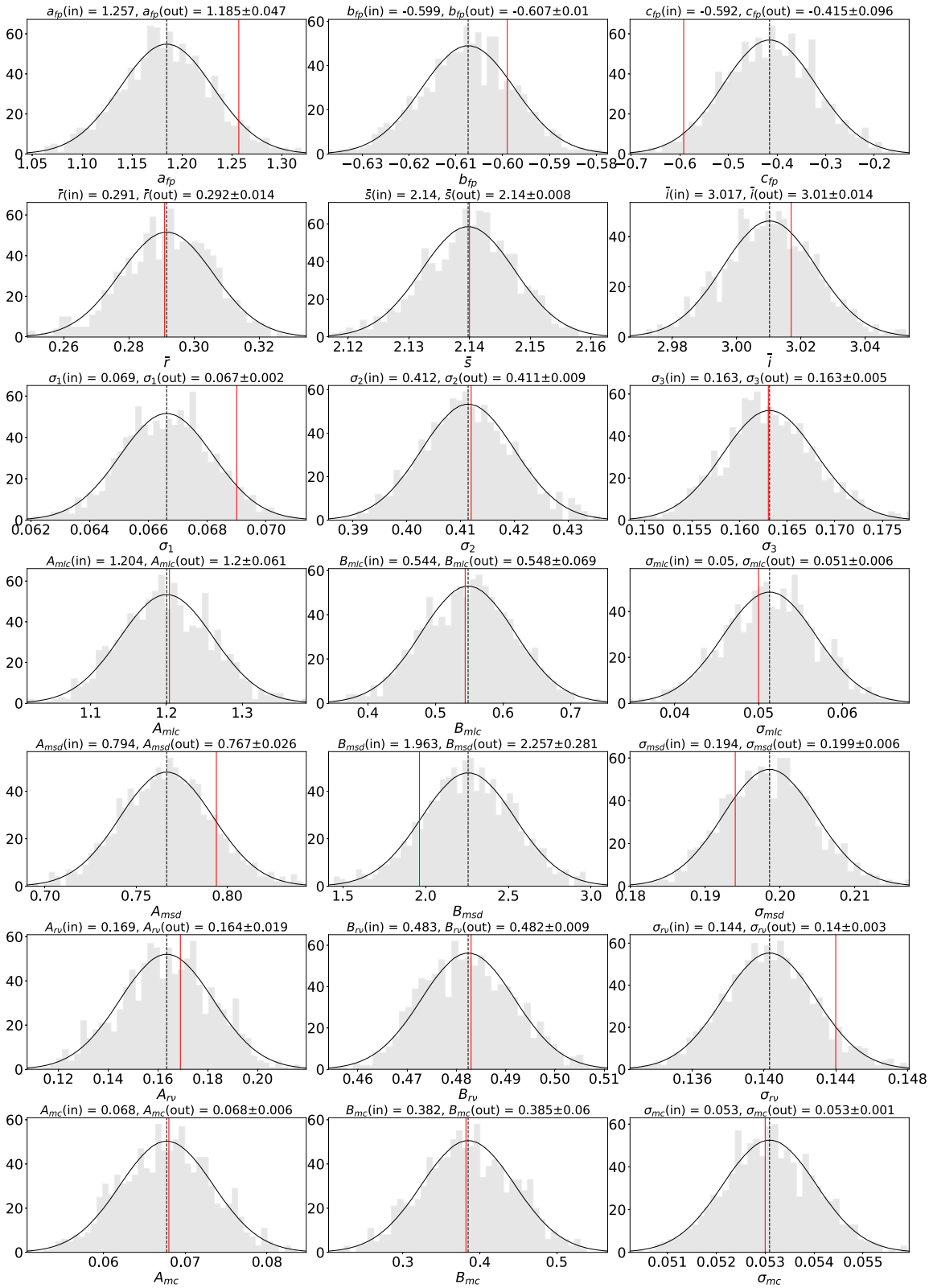

Figure 18. Distributions of the fitted parameters obtained from 1000 simulations of the best-fitting model for Qs. The first three rows show the FP parameters, the remaining four rows show the slopes, intercepts, and intrinsic scatters of the scaling relations mass-to-light vs. $g - i$ stellar mass (mc), respectively. The best-fitting Gaussian to the distribution for each parameter is shown by the black curve. The vertical dashed line shows the mean fitted value, and the vertical red line shows the input value. Each panel is centered on the mean, and the x-axis spans $\pm 3\sigma$.

Additionally, at the top of each panel, we give the input value and the fitted mean value along with the standard deviation, which provides the error estimate of the relevant parameter. Figure 18 shows that our 8D Gaussian model is statistically rigorous and provides a good description of the 8D parameter space, recovering all 20 input parameters

without major biases. We note that for cosmological applications, these simulations could be used to calibrate and correct for such biases, as in Magoulas et al. (2012), but we have not done so here.

Appendix D
Derivation of the Normalization Factor

In this appendix, we show how to derive an expression for the normalization factor f_j in Equation (22), in terms of CDF and PDF of Gaussians, that not only makes efficient sampling possible in `PySTAN` , but also makes the calculations faster using the corresponding optimized functions in `SciPy` instead of numerical integration which is much slower.

Considering the integration limits given in Equation (23), the normalization integral in Equation (22) becomes

$$f_j = \int_{u_{\mathrm{cut},j}}^{\infty} du_j \int_{s_{\mathrm{low}}}^{s_{\mathrm{up}}} ds_j \int_{-\infty}^{\infty} di_j d\nu_j dc_j \times p(u_j, s_j, i_j, \nu_j, c_j|\bar{\boldsymbol{w}}, \mathbf{C}_j^w). \tag{D1}$$

Since no cutoffs are applied to $\boldsymbol{i}$, $\boldsymbol{\nu}$, and $\boldsymbol{c}$, this integral is just the marginalization of the 5D PDF over these parameters,

$$\int_{-\infty}^{\infty} p(\boldsymbol{w_j}|\bar{\boldsymbol{w}}, \mathbf{C}_j^w) di_j d\nu_j dc_j = p(u_j, s_j|\bar{\boldsymbol{w}'}, \boldsymbol{C'}_j^w), \tag{D2}$$

which results in the bivariate Gaussian distribution of $\boldsymbol{w_j'} = (u_j, s_j)^\top$, where the mean vector is $\bar{\boldsymbol{w}'} = (\bar{u}, \bar{s})^\top = (\bar{i} + 2\bar{r}, \bar{s})^\top$ while the covariance matrix $\boldsymbol{C'}_j^w$ can be obtained by just striking out the rows and columns of $\mathbf{C}_j^w$ corresponding to $\boldsymbol{i}$, $\boldsymbol{\nu}$, and $\boldsymbol{c}$. Equation (D1) now becomes

$$f_j = \int_{u_{\mathrm{cut},j}}^{\infty} \int_{s_{\mathrm{low}}}^{s_{\mathrm{up}}} \frac{\exp\left[-\frac{1}{2}(\boldsymbol{w_j'} - \bar{\boldsymbol{w}'})^\top (\boldsymbol{C'}_j^w)^{-1} (\boldsymbol{w_j'} - \bar{\boldsymbol{w}'})\right]}{2\pi\sqrt{|\boldsymbol{C'}_j^w|}} du_j ds_j. \tag{D3}$$

Using the Cholesky decomposition of $\boldsymbol{C'}_j^w = L_j L_j^\top$ in Equation (D3), the exponent can be written as

$$\begin{aligned}\chi_j^2 &= (\boldsymbol{w_j'} - \bar{\boldsymbol{w}'})^\top (L_j L_j^\top)^{-1} (\boldsymbol{w_j'} - \bar{\boldsymbol{w}'}) \\ &= (\boldsymbol{w_j'} - \bar{\boldsymbol{w}'})^\top (L_j^{-1})^\top L_j^{-1} (\boldsymbol{w_j'} - \bar{\boldsymbol{w}'}) \\ &= [L_j^{-1}(\boldsymbol{w_j'} - \bar{\boldsymbol{w}'})]^\top [L_j^{-1}(\boldsymbol{w_j'} - \bar{\boldsymbol{w}'})].\end{aligned} \tag{D4}$$

Here, the lower triangular Cholesky factor L_j and its inverse L_j^{-1} are

$$L_j = \begin{pmatrix} L_{j,11} & 0 \\ L_{j,21} & L_{j,22} \end{pmatrix}, \; L_j^{-1} = \begin{pmatrix} \frac{1}{L_{j,11}} & 0 \\ \frac{-L_{j,21}}{L_{j,11}L_{j,22}} & \frac{1}{L_{j,22}} \end{pmatrix} \equiv \begin{pmatrix} H_{11} & 0 \\ H_{21} & H_{22} \end{pmatrix}. \tag{D5}$$

Then,

$$\begin{aligned}Q_j \equiv L_j^{-1}(\boldsymbol{w_j'} - \bar{\boldsymbol{w}'}) &= \begin{pmatrix} H_{11} & 0 \\ H_{21} & H_{22} \end{pmatrix} \begin{pmatrix} u_j - \bar{u} \\ s_j - \bar{s} \end{pmatrix} \\ &= \begin{pmatrix} H_{11}(u_j - \bar{u}) \\ H_{21}(u_j - \bar{u}) + H_{22}(s_j - \bar{s}) \end{pmatrix} = \begin{pmatrix} Q_{j,1} \\ Q_{j,2} \end{pmatrix}.\end{aligned} \tag{D6}$$

Inserting Equations (D6) into (D4), then renaming the constants result in

$$\begin{aligned}\chi_j^2 = Q_j^\top Q_j &= (Q_{j,1}, Q_{j,2}) \begin{pmatrix} Q_{j,1} \\ Q_{j,2} \end{pmatrix} = Q_{j,1}^2 + Q_{j,2}^2 \\ &= \underbrace{(H_{11}^2 + H_{21}^2)}_{2A_1^2}(u_j - \bar{u})^2 + 2\underbrace{H_{21}H_{22}}_{A_2}(u_j - \bar{u})(s_j - \bar{s}) \\ &\quad + \underbrace{H_{22}^2}_{2A_3^2}(s_j - \bar{s}).\end{aligned} \tag{D7}$$

Substituting Equation (D7) along with $|\mathbf{C'}_j^w| = |L_j L_j^\top| = |L_j|^2 = (L_{j,11}L_{j,22})^2$ in the integral (Equation (D3)) gives

$$\begin{aligned}f_j &= \int_{u_{\mathrm{cut},j}}^{\infty} \int_{s_{\mathrm{cut}}}^{\infty} \frac{e^{-[A_1^2(u_j-\bar{u})^2 + A_2(u_j-\bar{u})(s_j-\bar{s}) + A_3^2(s_j-\bar{s})^2]}}{2\pi L_{j,11}L_{j,22}} ds_j du_j \\ &= \frac{1}{2\pi L_{j,11}L_{j,22}} \int_{u_{\mathrm{cut},j}}^{\infty} e^{-A_1^2(u_j-\bar{u})^2} \times \left[\int_{s_{\mathrm{low}}}^{s_{\mathrm{up}}} e^{-A_3^2(s_j-\bar{s})^2 - A_2(u_j-\bar{u})(s_j-\bar{s})} ds_j\right] du_j \; .\end{aligned} \tag{D8}$$

The integral over s is in the form of

$$\int e^{-ax^2-bx} dx = \frac{1}{2}\sqrt{\frac{\pi}{a}} e^{b^2/4a} \,\mathrm{erf}\left[\sqrt{a}\left(x + \frac{b}{2a}\right)\right] \text{ for } a > 0, \tag{D9}$$

where erf is the error function. Therefore, for $a = A_3^2 > 0$ and $b = A_2(u_j - \bar{u})$, the inner integral over s becomes

$$I_s = \frac{1}{2}\sqrt{\frac{\pi}{a}} e^{b^2/4a} \,\mathrm{erf}\left[\sqrt{a}\left((s_j - \bar{s}) + \frac{b}{2a}\right)\right]_{s_{\mathrm{low}}}^{s_{\mathrm{up}}}. \tag{D10}$$

The error function can be expressed as $\mathrm{erf}(x) = 2\Phi(x\sqrt{2}) - 1$, where

$$\begin{aligned}\Phi(x) &= \frac{1}{\sqrt{2\pi}} \int_{-\infty}^{x} e^{-t^2/2} dt \\ &= \int_{-\infty}^{x} \phi(t) dt \text{ and } \phi(x) = \frac{d\Phi(x)}{dx}.\end{aligned} \tag{D11}$$

Then, Equation (D11) becomes

$$I_s = \sqrt{\frac{\pi}{a}} e^{b^2/4a} \Phi\left[\sqrt{2a}\,(s_j - \bar{s}) + \frac{b}{\sqrt{2a}}\right]_{s_{\mathrm{low}}}^{s_{\mathrm{up}}}. \tag{D12}$$

Plugging Equation (D12) into Equation (D8) along with the values of a and b constants:

$$f_j = \frac{\sqrt{\pi}}{2\pi L_{j,11} L_{j,22} A_3} \int_{u_{\mathrm{cut},j}}^{\infty} e^{-\left[A_1^2 - \frac{A_2^2}{4A_3^2}\right](u_j-\bar{u})^2} \Phi \times \left[\sqrt{2}A_3(s_j - \bar{s}) + \frac{A_2(u_j-\bar{u})}{\sqrt{2}A_3}\right]_{s_{\mathrm{low}}}^{s_{\mathrm{up}}} du_j. \quad \text{(D13)}$$

The definitions of the constants A_1, A_2, and A_3 from Equations (D7) and (D5) are

$$\begin{aligned} A_1^2 &= \frac{H_{11}^2 + H_{21}^2}{2} = \frac{1}{2L_{j,11}^2} + \left(\frac{-L_{j,21}}{2L_{j,11}L_{j,22}}\right)^2, \\ A_2 &= H_{21}H_{22} = \frac{-L_{j,21}}{L_{j,11}L_{j,22}^2}, \\ A_3^2 &= \frac{H_{22}^2}{2} = \frac{1}{2L_{j,22}^2} \Rightarrow \sqrt{2}A_3 = \frac{1}{L_{j,22}}, \\ A_1^2 &- \frac{A_2^2}{4A_3^2} = \frac{H_{11}^2 + H_{21}^2}{2} - \frac{H_{21}^2 H_{22}^2}{2H_{22}^2} = \frac{H_{11}^2}{2} = \frac{1}{2L_{j,11}^2}. \end{aligned} \quad \text{(D14)}$$

Finally, plugging Equation (D14) into Equation (D13),

$$f_j = \frac{1}{\sqrt{2\pi}L_{j,11}} \int_{u_{\mathrm{cut},j}}^{\infty} e^{-\frac{(u_j-\bar{u})^2}{2L_{j,11}^2}} \times \Phi\left(\frac{s_j - \bar{s}}{L_{j,22}} - \frac{L_{j,21}}{L_{j,22}}\frac{u_j - \bar{u}}{L_{j,11}}\right)\Bigg|_{s_{\mathrm{low}}}^{s_{\mathrm{up}}} du_j \quad \text{(D15)}$$

and using the PDF of normal distribution, we can write

$$f_j = \frac{1}{L_{j,11}} \int_{u_{\mathrm{cut},j}}^{\infty} \phi\left(\frac{u_j - \bar{u}}{L_{j,11}}\right) \Phi \times \left(\frac{s_j - \bar{s}}{L_{j,22}} - \frac{L_{j,21}}{L_{j,22}}\frac{u_j - \bar{u}}{L_{j,11}}\right)\Bigg|_{s_{\mathrm{low}}}^{s_{\mathrm{up}}} du_j. \quad \text{(D16)}$$

We can make even further simplifications by making the following definitions:

$$\alpha_{j,\mathrm{up}} \equiv \frac{s_{\mathrm{up}} - \bar{s}}{L_{j,22}}, \quad \alpha_{j,\mathrm{low}} \equiv \frac{s_{\mathrm{low}} - \bar{s}}{L_{j,22}}, \quad \beta_j \equiv \frac{-L_{j,21}}{L_{j,22}}, \quad \text{(D17)}$$

with change of variables to $t_j = \frac{u_j - \bar{u}}{L_{j,11}} \Rightarrow dt_j = \frac{du_j}{L_{j,11}}$, $t_{\mathrm{cut,j}} = \frac{u_{\mathrm{cut},j} - \bar{u}}{L_{j,11}}$,

$$f_j = \int_{t_{\mathrm{cut,j}}}^{\infty} \phi(t_j)[\Phi(\alpha_{j,\mathrm{up}} + \beta_j t_j) - \Phi(\alpha_{j,\mathrm{low}} + \beta_j t_j)]dt_j. \quad \text{(D18)}$$

This integral cannot be expressed in a closed form; however, it can be broken down into

$$\int_{t_{\mathrm{cut,j}}}^{\infty} \phi(t_j)\Phi(\alpha + \beta t_j)dt_j = \int_{-\infty}^{\infty} \phi(t_j)\Phi(\alpha + \beta t_j)dt_j - \int_{-\infty}^{t_{\mathrm{cut,j}}} \phi(t_j)\Phi(\alpha + \beta t_j)dt_j. \quad \text{(D19)}$$

Using the tables provided by Owen (1980), the first integral on the right-hand side of Equation (D19) can be expressed in a closed form and the second integral can be expressed in terms of the CDF of the bivariate normal distribution as follows:

$$\int_{t_{\mathrm{cut,j}}}^{\infty} \phi(t_j)\Phi(\alpha + \beta t_j)dt_j = \Phi\left(\frac{\alpha}{\sqrt{1+\beta^2}}\right) - \mathrm{BvN}\left(\frac{\alpha}{\sqrt{1+\beta^2}}, t_{\mathrm{cut,j}}, \rho = \frac{-\beta}{\sqrt{1+\beta^2}}\right), \quad \text{(D20)}$$

where BvN is the CDF of the (standard) bivariate normal distribution with correlation ρ given by

$$\mathrm{BvN}(h, k, \rho) = \frac{1}{2\pi\sqrt{1-\rho^2}} \int_{-\infty}^{k}\int_{-\infty}^{h} \exp \times \left[-\frac{1}{2}\left(\frac{x^2 - 2\rho xy + y^2}{1-\rho^2}\right)\right] dxdy. \quad \text{(D21)}$$

and it can be numerically evaluated using the readily available algorithms such as the one of Boys (1989). Finally, after rearranging the definitions in Equation (D17) as

$$\begin{aligned} h_{j,\mathrm{up/low}} &\equiv \frac{\alpha_{j,\mathrm{up/low}}}{\sqrt{1+\beta_j^2}} = \frac{s_{\mathrm{up/low}} - \bar{s}}{\sqrt{L_{j,22}^2 + L_{j,11}^2}} \\ k_j &\equiv t_{\mathrm{cut,j}} = \frac{u_{\mathrm{cut},j} - \bar{u}}{L_{j,11}} \\ \rho_j &\equiv \frac{-\beta_j}{\sqrt{1+\beta_j^2}} = \frac{L_{j,21}}{\sqrt{L_{j,22}^2 + L_{j,11}^2}}, \end{aligned} \quad \text{(D22)}$$

we can insert the results from Equations (D19) and (D20) into Equation (D18), which gives us the final expression for f_j as follows:

$$f_j = \Phi(h_{j,\mathrm{up}}) - \mathrm{BvN}(h_{j,\mathrm{up}}, k_j, \rho_j) - \Phi(h_{j,\mathrm{low}}) + \mathrm{BvN}(h_{j,\mathrm{low}}, k_j, \rho_j). \quad \text{(D23)}$$

Notice that in case of $s_{\mathrm{up}} \to \infty$ this equation reduces to

$$f_j = 1 - \Phi(k_j) - \Phi(h_{j,\mathrm{low}}) + \mathrm{BvN}(h_{j,\mathrm{low}}, k_j, \rho_j). \quad \text{(D24)}$$

Given the upper limit that we adopted for velocity dispersion is $\sigma_e < 450$ km s^{-1}, Equations (D23) and (D24) differ by $\lesssim 10^{-4}$ for all j.

We present this exact solution for each galaxy in Figure 19, which shows the variation of the normalization factor f_j as a function of the proposed distance.

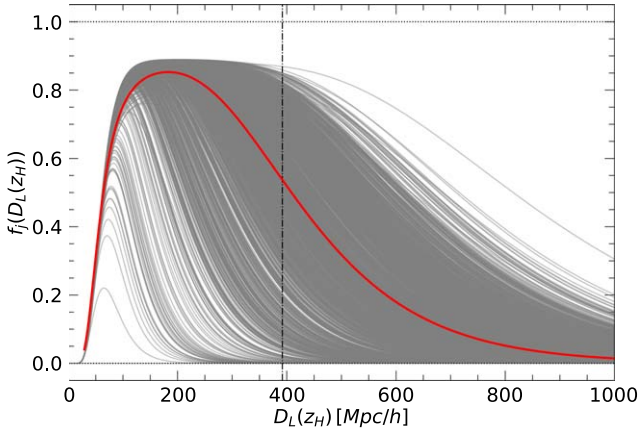

Figure 19. Normalization factor f_j as a function of luminosity distance (D_L) at the proposed cosmological redshift (z_H) for each Q galaxy in our sample. The thick red curve shows the median f_j. The vertical dashed–dotted line shows the luminosity distance corresponding to the redshift limit of our sample, $z = 0.12$.

Appendix E
PVs from Separate and Independent Modeling of the Samples

In this appendix, we make comparisons between the PVs derived from the FP and the MP, as we have done in Section 4.4, but for when the Q and SF galaxy samples are treated separately and independently. We present this comparison in Figures 20 and 21, which show that in this case, the FP and MH work approximately as well for both galaxy populations, with similar rms scatter and skewness for all measurements, and small but not necessarily negligible mean offsets between the alternative analysis. The skewness in these distributions, like those in Figures 13 and 14, is driven by a few outliers at very low η. Noting that in our FP/MH fitting such outliers are objectively identified and downweighted according to the good/bad mixture modeling, these points can be seen in, e.g., Figures 4, 5, and 7, as massive, red, and very high-velocity dispersion galaxies toward the upper end of our redshift window.

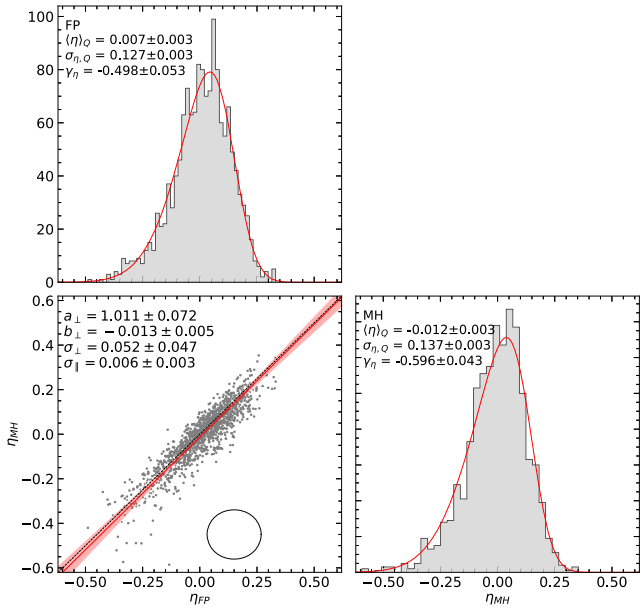

Figure 20. Same as Figure 13 but for Qs, when the Q and SF populations are modeled separately and independently.

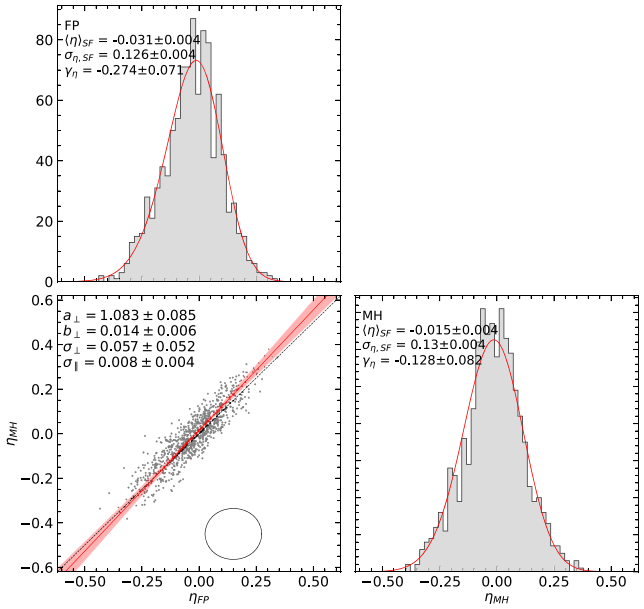

Figure 21. Same as Figure 20 but for the SFs.

ORCID iDs

M. Burak Dogruel https://orcid.org/0000-0002-8688-4331
Edward N. Taylor https://orcid.org/0000-0002-5522-9107
Michelle Cluver https://orcid.org/0000-0002-9871-6490
Matthew Colless https://orcid.org/0000-0001-9552-8075
Anna de Graaff https://orcid.org/0000-0002-2380-9801
Alessandro Sonnenfeld https://orcid.org/0000-0002-6061-5977
John R. Lucey https://orcid.org/0000-0002-9748-961X
Francesco D'Eugenio https://orcid.org/0000-0003-2388-8172
Cullan Howlett https://orcid.org/0000-0002-1081-9410
Khaled Said https://orcid.org/0000-0002-1809-6325

References

Abazajian, K. N., Adelman-McCarthy, J. K., Agüeros, M. A., et al. 2009, ApJS, 182, 543
Adams, C., & Blake, C. 2017, MNRAS, 471, 839
Aquino-Ortíz, E., Sánchez, S. F., Valenzuela, O., et al. 2020, ApJ, 900, 109
Baldry, I. K., Driver, S. P., Loveday, J., et al. 2012, MNRAS, 421, 621
Bell, E. F., McIntosh, D. H., Katz, N., & Weinberg, M. D. 2003, ApJS, 149, 289
Bernardi, M., Domínguez Sánchez, H., Margalef-Bentabol, B., Nikakhtar, F., & Sheth, R. K. 2020, MNRAS, 494, 5148
Bernardi, M., Sheth, R. K., Annis, J., et al. 2003, AJ, 125, 1866
Bertin, G., Ciotti, L., & Del Principe, M. 2002, A&A, 386, 149
Bezanson, R., Franx, M., & van Dokkum, P. G. 2015, ApJ, 799, 148
Blanton, M. R., & Moustakas, J. 2009, ARA&A, 47, 159
Boys, R. J. 1989, J. R. Stat. Soc. Ser. C (Appl. Stat.), 38, 580
Calcino, J., & Davis, T. 2017, JCAP, 2017, 038
Caon, N., Capaccioli, M., & D'Onofrio, M. 1993, MNRAS, 265, 1013
Cappellari, M. 2017, MNRAS, 466, 798
Cappellari, M., Bacon, R., Bureau, M., et al. 2006, MNRAS, 366, 1126
Cappellari, M., Scott, N., Alatalo, K., et al. 2013, MNRAS, 432, 1709
Carpenter, B., Gelman, A., Hoffman, M. D., et al. 2017, J. Stat. Softw., 76, 1
Carrick, J., Turnbull, S. J., Lavaux, G., & Hudson, M. J. 2015, MNRAS, 450, 317
Colless, M., Saglia, R. P., Burstein, D., et al. 2001, MNRAS, 321, 277
Cortese, L., Fogarty, L. M. R., Ho, I. T., et al. 2014, ApJL, 795, L37
Courteau, S., Cappellari, M., de Jong, R. S., et al. 2014, RvMP, 86, 47
Dam, L. 2020, MNRAS, 497, 1301
de Graaff, A., Bezanson, R., Franx, M., et al. 2020, ApJL, 903, L30
de Graaff, A., Bezanson, R., Franx, M., et al. 2021, ApJ, 913, 103

Djorgovski, S., & Davis, M. 1987, ApJ, 313, 59
Dogruel, M. B., Taylor, E. N., Cluver, M., et al. 2023, ApJ, 953, 45
Dressler, A., Lynden-Bell, D., Burstein, D., et al. 1987, ApJ, 313, 42
Falcón-Barroso, J., Sánchez-Blázquez, P., Vazdekis, A., et al. 2011, A&A, 532, A95
Graves, G. J., & Faber, S. M. 2010, ApJ, 717, 803
Graves, G. J., Faber, S. M., & Schiavon, R. P. 2009, ApJ, 698, 1590
Graziani, R., Courtois, H. M., Lavaux, G., et al. 2019, MNRAS, 488, 5438
Harrison, E. R. 1974, ApJL, 191, L51
Hong, T., Springob, C. M., Staveley-Smith, L., et al. 2014, MNRAS, 445, 402
Hopkins, A. M., Driver, S. P., Brough, S., et al. 2013, MNRAS, 430, 2047
Howlett, C., Said, K., Lucey, J. R., et al. 2022, MNRAS, 515, 953
Howlett, C., Staveley-Smith, L., Elahi, P. J., et al. 2017, MNRAS, 471, 3135
Hubble, E. 1929, PNAS, 15, 168
Hyde, J. B., & Bernardi, M. 2009, MNRAS, 396, 1171
Jones, D. H., Read, M. A., Saunders, W., et al. 2009, MNRAS, 399, 683
Jorgensen, I., Franx, M., & Kjaergaard, P. 1995, MNRAS, 276, 1341
Kaiser, N. 1987, MNRAS, 227, 1
Koda, J., Blake, C., Davis, T., et al. 2014, MNRAS, 445, 4267
Kourkchi, E., Tully, R. B., Eftekharzadeh, S., et al. 2020, ApJ, 902, 145
Lange, R., Driver, S. P., Robotham, A. S. G., et al. 2015, MNRAS, 447, 2603
Leavitt, H. S., & Pickering, E. C. 1912, HarCi, 173, 1
Magoulas, C., Springob, C. M., Colless, M., et al. 2012, MNRAS, 427, 245
Owen, D. B. 1980, Commun. Stat. - Simul. Comput., 9, 389
Phillips, M. M. 1993, ApJL, 413, L105
Qin, F., Parkinson, D., Howlett, C., & Said, K. 2021, ApJ, 922, 59
Riess, A. G., Casertano, S., Yuan, W., et al. 2021, ApJL, 908, L6
Riess, A. G., Macri, L. M., Hoffmann, S. L., et al. 2016, ApJ, 826, 56
Robotham, A. S. G., Norberg, P., Driver, S. P., et al. 2011, MNRAS, 416, 2640
Said, K., Colless, M., Magoulas, C., Lucey, J. R., & Hudson, M. J. 2020, MNRAS, 497, 1275
Sánchez-Blázquez, P., Peletier, R. F., Jiménez-Vicente, J., et al. 2006, MNRAS, 371, 703
Schmidt, M. 1968, ApJ, 151, 393
Scolnic, D. M., Jones, D. O., Rest, A., et al. 2018, ApJ, 859, 101
Springob, C. M., Magoulas, C., Proctor, R., et al. 2012, MNRAS, 420, 2773
Springob, C. M., Magoulas, C., Colless, M., et al. 2014, MNRAS, 445, 2677
Taylor, E. N., Franx, M., Brinchmann, J., van der Wel, A., & van Dokkum, P. G. 2010, ApJ, 722, 1
Taylor, E. N., Hopkins, A. M., Baldry, I. K., et al. 2011, MNRAS, 418, 1587
Taylor, E. N., Hopkins, A. M., Baldry, I. K., et al. 2015, MNRAS, 446, 2144
Taylor, E. N., Cluver, M., Bell, E., et al. 2023, Msngr, 190, 46
Tonry, J. L., Blakeslee, J. P., Ajhar, E. A., & Dressler, A. 2000, ApJ, 530, 625
Tully, R. B., Courtois, H., Hoffman, Y., & Pomarède, D. 2014, Natur, 513, 71
Tully, R. B., Courtois, H. M., & Sorce, J. G. 2016, AJ, 152, 50
Tully, R. B., & Fisher, J. R. 1977, A&A, 500, 105
Turnbull, S. J., Hudson, M. J., Feldman, H. A., et al. 2012, MNRAS, 420, 447
van der Wel, A., van Houdt, J., Bezanson, R., et al. 2022, ApJ, 936, 9
Watkins, R., & Feldman, H. A. 2015, MNRAS, 450, 1868
Weiner, B. J., Willmer, C. N. A., Faber, S. M., et al. 2006, ApJ, 653, 1027
Zaritsky, D., Zabludoff, A. I., & Gonzalez, A. H. 2008, ApJ, 682, 68
Zibetti, S., Charlot, S., & Rix, H.-W. 2009, MNRAS, 400, 1181